# Microwave Radiometer Calibration Using Deep Learning With Reduced Reference Information and 2-D Spectral Features

Ahmed Manavi Alam, *Graduate Student Member, IEEE*, Mehmet Kurum, *Senior Member, IEEE*, Mehmet Ogut, *Member, IEEE*, and Ali C. Gurbuz, *Senior Member, IEEE* 

Abstract—The accuracy of geophysical retrievals from radiometers relies on calibration quality, encompassing both absolute radiometric accuracy and spectral consistency. Radiometers have employed various calibration techniques, including external targets, vicarious sources, and internal calibrators like noise diodes or matched reference loads. Calibration techniques face challenges like frequency dependence, instrumental effects, environmental influences, drift, aging, and radio frequency interference. Recent hardware advancements enable radiometers to collect raw samples containing both temporal and spectral information. Leveraging advanced modeling techniques like deep learning (DL) enables detecting subtle correlations, non-linear dependencies, and higherorder interactions within the data extracting valuable information that may have been challenging with conventional methods. This study utilizes NASA's Soil Moisture Active Passive (SMAP) satellite's level 1A and level 1B data products to develop a DL-based radiometer calibrator to estimate antenna temperature. Spectrograms of second raw moments equivalent to power carrying the 2-D spectral features serve as primary input in a supervised convolutional neural network-based architecture. DL-based calibrator has demonstrated high correlation and low root mean square error when incorporating spectral information from both reference and noise diodes and when not considering this information. Findings suggest that the ancillary features such as internal thermistor temperature and loss elements exhibit sufficient accuracy in estimating antenna temperature to compensate for variations in receiver noise temperature and short-term gain fluctuations in the absence of the reference load and noise diode power. The proposed calibration technique with reduced reference information might enable radiometers for a higher number of antenna scene observations within a footprint.

Index Terms—Calibration, deep learning (DL), machine learning, microwave radiometry, neural network, radio frequency interference (RFI), soil moisture active passive (SMAP).

Manuscript received 31 July 2023; revised 30 September 2023 and 2 November 2023; accepted 5 November 2023. Date of publication 15 November 2023; date of current version 4 December 2023. This work was supported in part by the National Science Foundation under Grant 2030291 and Grant 2047771 and in part by the Jet Propulsion Laboratory, California Institute of Technology under a contract with the National Aeronautics and Space Administration under Grant 80NM0018D0004. (Corresponding author: Ali C. Gurbuz.)

Ahmed Manavi Alam and Ali C. Gurbuz are with the Department of Electrical and Computer Engineering, and Information Processing and Sensing Lab, Mississippi State University, Mississippi State, MS 39672 USA (e-mail: aa2863@msstate.edu; gurbuz@ece.msstate.edu).

Mehmet Kurum is with the School of Electrical and Computer Engineering, University of Georgia, Athens, GA 30602 USA (e-mail: kurum@uga.edu).

Mehmet Ogut is with the Jet Propulsion Laboratory, California Institute of Technology, Pasadena, CA 91109 USA (e-mail: mehmet.ogut@jpl.nasa.gov).

Digital Object Identifier 10.1109/JSTARS.2023.3333268

#### I. INTRODUCTION

ICROWAVE and millimeter wave radiometry has played a vital role in advancing our understanding of the distribution and dynamics of geophysical parameters, such as soil moisture, sea-surface wind, ocean salinity, atmospheric water vapor, freeze/thaw state, and snow water equivalent [1], [2], [3]. These instruments have proven to be extremely valuable across diverse fields, including hydrology, agriculture, meteorology, climatology, and oceanography. Evaluating the performance of a radiometer involves considering various crucial factors, such as accuracy and sensitivity. Accuracy directly impacts the reliability of the parameters derived from radiometric measurements. Conversely, radiometric resolution or sensitivity determines the smallest detectable change in a radiometer's readings, accounting for its internal noise [4], [5]. Sensitivity plays a crucial role in microwave radiometry according to the requirement of observed geophysical parameters. Consequently, enhancing accuracy and radiometric resolution contributes to higher-quality geophysical data derived from radiometric measurements [6].

Microwave radiometers employ various calibration methods to achieve precise and dependable measurements of microwave radiation. These calibration techniques are designed to enhance the accuracy and reliability of the collected data. Calibration techniques can be categorized into two distinct parts: external calibration and internal calibration [7]. This end-to-end calibration is widely used to estimate antenna temperature in microwave radiometers [1]. External calibration technique involves using external references or targets in space to calibrate the radiometer's measurements. This involves well-characterized radiometric properties of two known targets and can be used as a reference to produce a voltage-to-antenna temperature calibration line. However, challenges include accessing stable calibration references, variations in environmental conditions, instrument stability within the calibration cycle, and correcting fast 1/f noise gain fluctuations [4], [8].

Radiometer internal calibration includes noise injection and Dicke-switching reference loads. By employing a fast switching between internal calibration sources, the gain fluctuation resulting from 1/f noise at the receiver output can be effectively eliminated. This calibration technique assumes that the output voltage is linearly related to the noise temperature of the input source. However, in practice, the calibration of internal

calibrators may introduce measurement uncertainty attributed to various factors, including noise diode instability arising from thermal fluctuations and aging, as well as potential mismatches at the reference load [9]. These factors can introduce errors or biases in the calibration, leading to inaccuracies in the radiometric measurements [6], [10], [11]. This study proposes a new calibration technique based on deep learning (DL) that will utilize: 1) 2-D time-frequency spectral features and 2) reduced reference information from reference and noise sources to estimate antenna temperature. The utilization of the DL method shows promising potential in reducing the need for frequent internal calibration, thereby facilitating an increased frequency of antenna temperature measurements. Following the launch, samples collected from vicarious sources or other calibration targets can be employed to tune the DL-based calibration of the instrument during on-orbit operation. This adjustment might be crucial in accommodating on-orbit effects, nonstationary instrument changes, such as aging and orbital variations.

Data-driven approaches have been recently introduced for the calibration of radiometers, as demonstrated in the works of authors in [12] and [13]. These studies employed both simulated and airborne microwave radiometer instruments to evaluate the effectiveness of the proposed techniques. Both of these studies utilized an artificial neural network (ANN) framework to estimate antenna temperature from the radiometer output voltages. Different training scenarios are utilized to understand the dependence on reference loads and noise diodes (ND). The input features consist of average voltage for a particular footprint or antenna temperature estimation. However, radiometers are moving toward wideband sensing in the unprotected region, so it is important to leverage spectral information [14]. Radiometers are collecting time-frequency 2-D data, which is not directly used in calibration. The proposed approach of this study will be using those 2-D features along with different ancillary information for the calibration to examine the robustness with reduced reference information. Different validation strategies will be employed to understand the generalization capability of DL in estimating antenna temperature.

This article presents a novel DL-based calibration framework that aims to accurately estimate antenna temperature using spectrograms, which are 2-D time-frequency spectral features derived from raw antenna counts or voltages. In addition, the framework incorporates temperature and losses information from radiometer elements to enhance the calibration performance. Convolutional neural networks (CNNs) along with fully connected layers have been utilized to model the relationship between the input voltage and output antenna temperatures. The input consists of several primary and secondary features to help with data-driven modeling. To understand, how much information the DL-based calibrator needs from the ND and reference load, we demonstrate different training and testing scenarios. NASA's Soil Moisture Active Passive (SMAP) satellite's level 1A and level 1B data products are utilized as the dataset [15], [16], [17]. Level 1A antenna counts are used as inputs of the DL-model and level 1B antenna temperatures are used as the label temperature/ ground truth information [18], [19]. In order to assess the robustness and effectiveness of our

TABLE I YEAR WISE DATA STATISTICS FOR CALIBRATION

Year	Total Samples	Usable for DL	Land: Land-Water (%)
2017	54,819,788	47,241,275	17.76
2018	49,281,487	38,854,325	17.62
2019	51,411,623	39,611,521	17.82
2020	52,112,242	41,124,791	17.75
2021	53,619,032	43,158,189	17.79
2022	52,235,101	44,431,891	17.77
Total	313,479,273	255,421,992	17.74

model within a new time frame, we trained it using data from a specific year and evaluated its performance using data from different years. The occurrence of gain fluctuations necessitates frequent internal calibration. However, the employment of the DL method holds promise in reducing the frequency of internal calibration, thereby enabling a greater number of antenna temperature measurements. This study's DL-based framework provides better performance than previous ANN-based models with additional cross-validation (CV) techniques to portray the robustness [12], [13].

The rest of this article is organized as follows. Details of the utilized SMAP data statistics, dataset preparation, and example spectrograms are discussed in Section II. Section III details the preprocessing on data, the proposed DL architecture, training of the DL architecture and evaluation metrics of DL models. Results and discussions are provided in Section IV and V, respectively. Finally, Section VI concludes this article.

#### II. DATASET

In this study, the development of a DL-based calibration unit is realized on the utilization of level 1A and level 1B data products from SMAP. These data products serve as the foundation for training and implementing the calibration framework. SMAP is an Earth observation satellite that provides  $36 \times 47 \text{ km}^2$  spatial resolution and takes about 2–3 days to complete global coverage. The SMAP satellite was successfully launched on 31 January, 2015, and has since been a valuable source of essential scientific data products contributing significantly to Earth observation and weather prediction endeavors [20], [21], [22], [23]. Data products for this study are taken from the year 2017 to 2022 to perform the training and testing of the algorithm. In the following sections, we will demonstrate data statistics along with which features are chosen from SMAP level 1A and level 1B data products to train the DL model. This will be followed by data preparation, data statistics, and training scenarios.

## A. Data Statistics

Table I gives the overall data statistics. Total 313 million samples or footprints from SMAP are considered in this study. In data-driven modeling approaches it is important to ensure the quality and reliability of the data products. Quality flags from SMAP level 1B are used to ensure the consistency in data. SMAP contains different quality flags, such as range flag—which ensures data temperature value is not out of range, acceptable quality flag—which confirms the acceptable quality

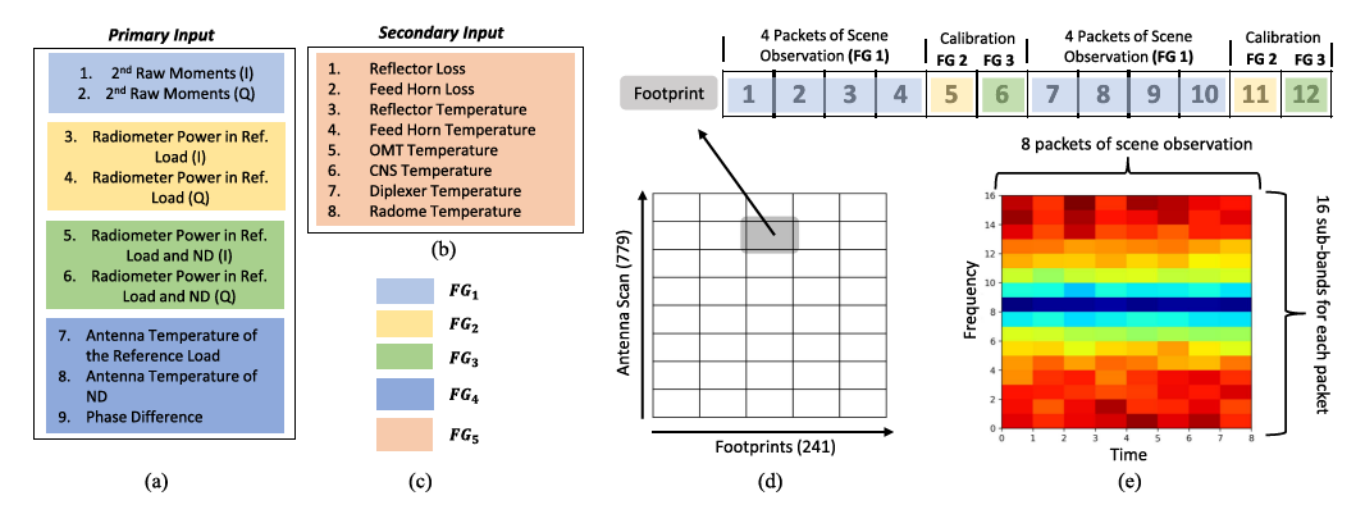


Fig. 1. Illustration of input features for DL-based radiometer calibration. (a) 2-D  $(16 \times 8)$  primary inputs. (b) Scalar secondary inputs. (c) Five FG for different training/testing scenarios illustrated with colors. (d) SMAP data structure for a particular HDF5 file and corresponding switching sequence of a particular footprint. (e) Overall spectrogram of a particular footprint comprises eight antenna measurements and 16 subbands for each antenna measurement.

of the measurements, RFI detection flag—whether a footprint is RFI contaminated or not, and NEDT flag—footprints have acceptable radiometric resolution. These flags contribute to the selection of approximately 255 million samples over a span of six years, which can be effectively utilized for DL input purposes. Using footprint surface status these samples are further divided into land (ground only) and land—water mix (containing both ground and water) samples. The ratio between land and land—water ranges from 17.6% to 17.8%. Input features for DL-based calibration are shown in Fig. 1, which will be discussed further in the following sections.

#### B. SMAP Level 1A Data

The SMAP level 1A data product comprises antenna counts at both full-band and subband levels [16], [18]. These antenna counts are represented by the first, second, third, and fourthorder statistical raw moments. In this study, the second raw moments hold particular significance as they can be treated as an equivalent measure of power. Therefore, the second raw moments serve as the primary input for the analysis conducted in this research. Fig. 1(a) lists the features extracted from level 1A data product. In addition, input features in this study include the measured counts of the reference load and the reference plus ND. These reference counts provide valuable information and are utilized alongside the raw antenna moments for the analysis conducted in this research. All of these moments are available in both the in-phase (I) and quadrature (Q) channels for both the horizontal polarization (H-pol) and vertical polarization (V-pol). The precise delineation of variable definitions within SMAP level 1A products is comprehensively outlined in Table II. This table consists of the information used for DL-based calibration and corresponding data name fields in SMAP. It also provides a description of how SMAP stores that particular data field. The modifications applied to the input features for the DL-based framework will be comprehensively explained in Section II-D of this article.

#### C. SMAP Level 1B Data

The level 1B data products consist of antenna temperature measurements, quality flags indicating data reliability, and loss elements pertaining to various radiometer components [17], [19]. The features are presented and listed in Fig. 1(a) and (b), respectively. In this study, the antenna temperature values of both the H-pol and V-pol are utilized as ground truth references. These measurements are employed to model the relationship between the measured input voltage and the resulting antenna temperature. To help with the calibration, thermistor data from the reference load and ND physical temperature are also taken as input features to the model. The model also incorporates thermistor/ physical temperature readings from various components of the satellite, including the reflector, feed horn, orthomode transducer (OMT), and correlated noise source (CNS) for training. Loss elements of different components are crucial in calibrating radiometers and loss elements, such as reflector loss, feed horn loss, and phase imbalances are also taken from SMAP level 1B data products. More details about these features can be found in the algorithm theoretical basis document of SMAP [24]. The comprehensive elucidation of variable definitions within SMAP level 1A and level 1B product is provided in Table II. The first column shows the inputs utilized in the DL-based calibration. The second column illustrates the corresponding data name fields in SMAP level 1A and level 1B user guides [16], [17]. The description of the data field is depicted in the third column. The subsequent section will showcase the data preparation process for a DL-based calibrator, employing level 1A and level 1B data products.

## D. Data Preparation

Input features utilized in the DL-based calibrator are divided into primary and secondary groups as illustrated in Fig. 1(a) and 1(b). The primary inputs consist of 2-D time-frequency spectrograms, which are directly fed into the convolutional layers of the DL model. In addition, secondary inputs comprise

TABLE II
SMAP LEVEL 1A AND LEVEL 1B DATA USED FOR DL-BASED CALIBRATION [16], [17]

Inputs for DL-Based	Data Name Field In SMAP	Description					
Calibration DL-Based	Dam Tune Hou in SWAI	aredesignions					
2nd Raw Moments (I)	m2 16 ant	The second raw moment in each packet of sub-band radiometer data in the antenna state. Both V-pol and H-pol are separated into their in-phase and quadrature components.					
2nd Raw Moments (Q)	mz_ro_ant						
Radiometer Power in Ref. Load (I)	m2_16_ref	The second raw moment of sub-band radiometer data in the reference state. Both V-pol and H-pol are separated into their in-phase and quadrature components.					
Radiometer Power in Ref. Load (Q)	mz_ro_rei						
Radiometer Power in Ref. Load and ND (I)	m2 16 ref nd	The second raw moment of sub-band radiometer data in the reference plus internal noise diode					
Radiometer Power in Ref. Load and ND (Q)	mz_ro_rei_nd	state. Both V-pol and H-pol are separated into their in-phase and quadrature components.					
Antenna Temperature of	cal_temp_ref	Physical temperature of reference load. Stored as V-pol and H-pol.					
the Reference Load	cal_tempref_offset16	Physical temperature offset for reference load. This is divided into sub-band radiometer data and separated into V-pol and H-pol.					
Antenna Temperature of ND	cal_temp_nd16	Physical temperature for ND. This is divided into sub-band radiometer data and separated into V-pol and H-pol.					
Phase Difference	cal_xnd_phase16	External noise diode phase. This is divided into sub-band radiometer data and separated into V-pol and H-pol.					
Reflector Loss	cal_loss1_reflector	Loss factor of reflector. Stored as V-pol and H-pol.					
Feed Horn Loss	cal_loss2_feed16	Loss factor of feed. Stored as V-pol and H-pol.					
Reflector Temperature	cal_temp1_reflector	Physical temperature of reflector. Stored as V-pol and H-pol.					
Feed Horn Temperature	cal_temp2_feed	Physical temperature of feed. Stored as V-pol and H-pol.					
OMT Temperature	cal_temp3_omt	Physical temperature of OMT. Stored as V-pol and H-pol.					
CNS Temperature	cal_temp4_coupler	Physical temperature of CNS. Stored as V-pol and H-pol.					
Diplexer Temperature	cal_temp5_diplexer	Physical temperature of diplexer. Stored as V-pol and H-pol.					
Radome Temperature	cal_temp12_radome	Physical temperature of radome. Stored as V-pol and H-pol.					
Antenna Temperature	ta_filtered_v	V-pol antenna temperature after RFI filtering.					
Amenna Temperature	ta_filtered_h	H-pol antenna temperature after RFI filtering.					
Quality Flags	tb_qual_flag_v	Bit flags that indicate the quality of the V-pol brightness temperature.					
Quanty Flags	tb_qual_flag_h	Bit flags that indicate the quality of the H-pol brightness temperature.					
Footprint Status	footprint_surface_status	Indicates if the footprint center lies on land (0) or water (1).					

single-valued features that are combined inside DL-framework with the extracted features from the primary input. These inputs are divided into five different feature groups (FGs) shown in Fig. 1(c) to find the opportunistic solution to calibrate radiometers with or without the power information from reference and ND. FG<sub>1</sub> contains the features of 2nd raw moments equivalent to power of observed scene. FG<sub>2</sub> and FG<sub>3</sub> contains the power of reference load and ND, respectively. These two FGs are crucial to implementing a linear relationship between the temperature and power of the radiometer. FG4 contains the internal physical temperature of reference and ND and FG<sub>5</sub> contains the element losses and physical temperatures. FGs are categorized according to their distinct roles within the radiometer. Five different FGs will help to create different training scenarios for DL (detailed in Section II-E). Among all the FGs, FG<sub>1</sub> consists of antenna counts information,  $FG_2$  and  $FG_3$  provide reference counts information. FG<sub>4</sub> and FG<sub>5</sub> offer internal temperature, loss elements, and phase information of reference and radiometer components. Switching of the radiometer for a particular footprint along with SMAP data structure for a particular HDF5 file is illustrated in Fig. 1(d). A radiometer footprint is defined as a sequence of 12 packets and each packet corresponds to a time duration of 1.2 ms.

Within this sequence, eight packets are dedicated to observing the scene grouped with FG<sub>1</sub>, while the 5th, 6th, 11th, and 12th packets are specifically allocated for internal calibration purposes grouped with FG2 and FG3. Each packet contains 1.2 ms of radiometer data integration and they are divided into 16 subbands where each subband covers a band of 1.5 MHz forming the total SMAP radiometer band of 1400–1427 MHz. Primary inputs illustrated in Fig. 1 are 2-D spectrograms with a shape of  $16 \times 8$ . Fig. 1(e) illustrates an example antenna count spectrogram of a particular footprint comprising 8 antenna measurements and 16 subbands. A particular radiometer footprint consists of two packets of reference and two packets of reference plus ND. To accommodate a consistent matrix size for the DL model, we have broadcasted these observations into  $16 \times 8$ rather than  $16 \times 2$ . The broadcasting process involves extending the same reference packet for four consecutive packets within a specific subband.

Spectrograms of these input features are demonstrated in Fig. 2. Second raw moments of I and Q channels are illustrated in Fig. 2(a) and 2(b). These spectrograms show how a particular antenna footprint comprises 8-time windows and 16 frequency subband measurements. Spectrograms of reference load (I and

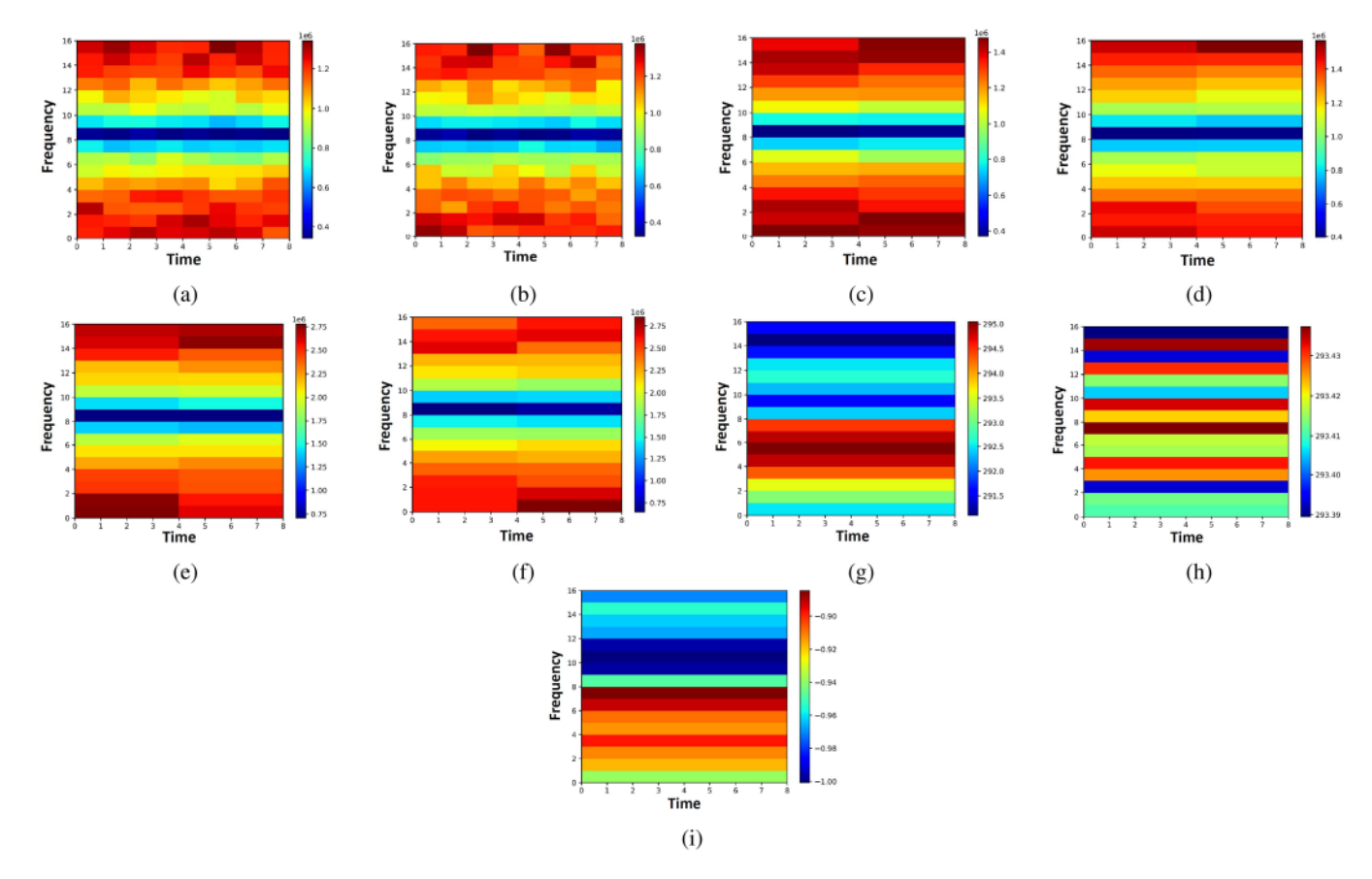


Fig. 2. Example spectrograms generated from level 1A and level 1B data products for a particular footprint. Antenna counts of (a) second raw moments (I), (b) second raw moments (Q), (c) reference load (I), (d) reference load (Q), (e) Reference load and ND (I), (f) reference load and ND (Q), (g) reference load physical temperature, (h) ND physical temperature, and (i) phase. The spectrograms were acquired using vertical polarization.

Q) and reference load plus ND (I and Q) are depicted in Fig. 2(c)— (f), respectively. As mentioned previously there are two packets of reference load power for a particular radiometer footprint and these are converted into  $16 \times 8$  spectrograms to accommodate directly into the DL-based framework. Fig. 2(g)-(i) illustrate the physical temperature of reference load, physical temperature of ND, and phase difference, respectively. These nine different 2-D primary input (see Fig. 1) features are combined to create a new image with a tensor of  $16 \times 8 \times 9$ . Secondary inputs are a single numerical value for each footprint and incorporating them in a DL-based calibrator helps to increase the performance by addressing instrument attributes. Nine-channel  $16 \times 8$  tensor helps to map a relationship between antenna temperatures and antenna counts spectrograms by extracting important features through a DL-based framework. This study's novel framework offers enhanced flexibility and capability by learning features from 2-D spectral inputs and combining them with single-value loss and temperature elements. This is completely different than previous architectures based on ANNs [12] that utilize single-value power feature inputs.

# E. Training Scenarios

From the previous section, we have seen all the input features are divided into five major FG in accordance with their functionality in a radiometer calibration. These FGs are used to develop various training and testing schemes for DL-based frameworks.

These training schemes are essential for determining the optimal amount of voltage or power information required from the reference unit to achieve an accurate estimation of antenna temperature. These training schemes are given below.

- 1) Case 1: All FG.
- 2) Case 2:  $FG_1 + FG_3 + FG_4 + FG_5$ .
- 3) Case 3:  $FG_1 + FG_2 + FG_4 + FG_5$ .
- 4) Case 4:  $FG_1 + FG_2^* + FG_3^* + FG_4 + FG_5$ .
- 5) *Case 5:*  $FG_1 + FG_4 + FG_5$ .

FG<sub>2</sub>\* and FG<sub>3</sub>\* represent using only the 5th and 6th time packet observation of FG2 and FG3. These training schemes for DL-based calibrators are illustrated in Fig. 3. Case 1 utilizes the same input features that are used in conventional radiometer calibration. As we are using SMAP's antenna temperature as ground truth, a direct comparison with the conventional approach is out of scope for this study. But future studies will incorporate this calibration method in airborne L-band radiometers to compare the performance. Case 2 will be using the information from ND and without matched reference load information. Case 3 is opposite to Case 2 using only reference load information. Case 4 utilizes one packet of reference and ND information whereas conventional calibration requires two packets of reference and ND information per radiometer footprint. Case 5 uses no power information from the reference load and ND. It is important to note that during our training process, we always incorporate FG<sub>1</sub>, FG<sub>4</sub>, and FG<sub>5</sub>. FG<sub>4</sub> contains the physical temperature feature of reference and ND. The findings from this analysis will

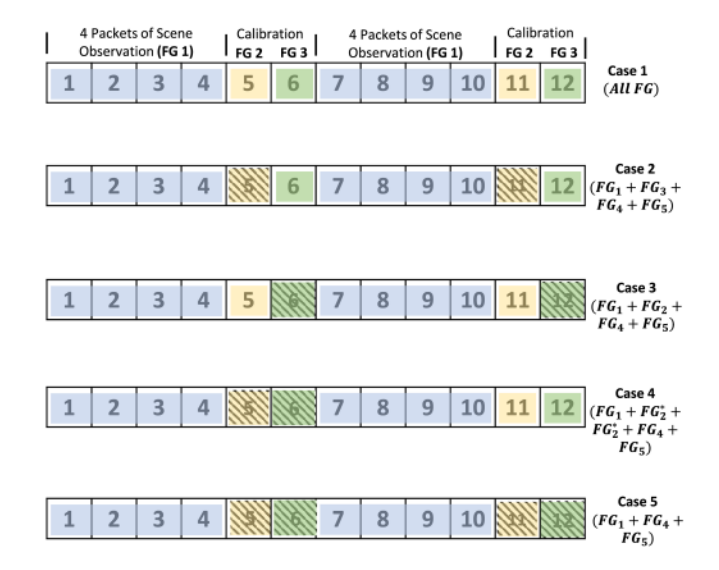


Fig. 3. Different training schemes for DL-based calibrator.

suggest that the thermistor temperature and loss elements exhibit sufficient stability to compensate for variations in receiver noise temperature and short-term gain fluctuations in the absence of the reference load and ND power.

Utilizing the footprint surface status quality flags, we have trained and tested our model with samples from only land and samples from the land—water combination. This flag indicates if the footprint center lies on land (0) or water (1). Training and testing with land and land—water combinations help to understand the spatial dependency of the DL-based models. V-pol antenna temperature of the samples showing different spatial distributions is depicted in Fig. 4. Samples from the land—water combination will be critical to understanding if there are any additional biases affecting the performance of the model. It will also help to understand if a higher dynamic temperature range in land—water mix samples has any impact on DL-based calibrator performance.

## III. METHODOLOGY

DL is an approach within machine learning that specifically emphasizes the utilization of neural networks with multiple layers that can learn and extract meaningful representations directly from raw data. DL has garnered substantial attention and popularity because of its remarkable capability to automatically learn hierarchical representations in tasks, such as image recognition, speech recognition, natural language processing, and various other domains. This section illustrates the overall structure and training of the DL-based framework to predict radiometer antenna temperature from SMAP level 1A and level 1B inputs. Data-driven approaches to estimate radiometer antenna temperature are first introduced in [12]. These studies examined the usage of single-point features in different scenarios, including cases with or without reference and ND voltages. However, the increasing adoption of wideband sensing in radiometers is driven by the growing applications involving various geophysical parameters [25], [26]. In addition, the presence of unwanted

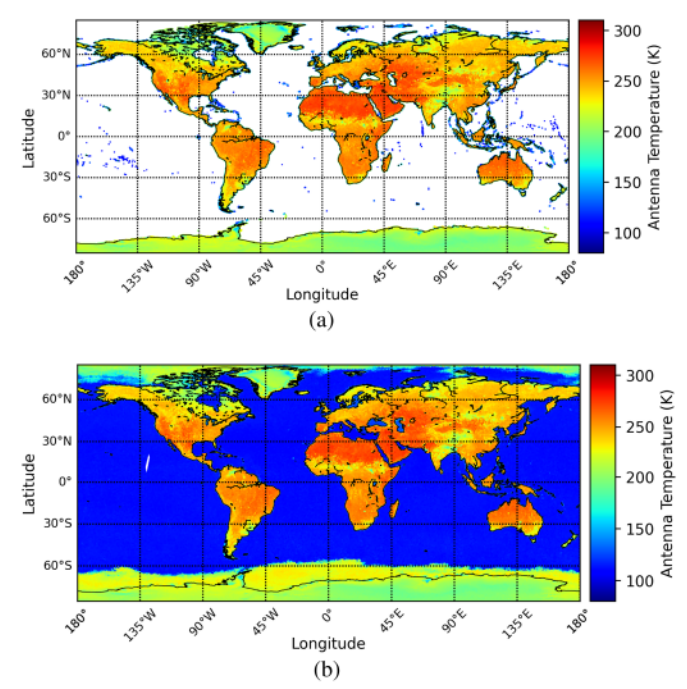


Fig. 4. Antenna temperature (V-pol) of the samples showing their spatial distribution over (a) land and (b) land-water mix. Antenna temperature is recorded from 17 October, 2021, to 27 October, 2021.

signals like RFI in observations has emphasized the significance of utilizing spectral features to achieve successful retrieval of desired information [27], [28], [29], [30], [31]. These 2-D spectral features consisting of both time and frequency features have not previously been utilized in data-driven radiometer calibration methods [12]. This study has implemented a novel CNN-based radiometer calibration unit that estimates the antenna temperature by leveraging 2-D antenna count spectrograms and combining learned features from CNN with secondary inputs. CNNs are designed to process and extract meaningful features from 2-D input data [32], [33], [34]. They employ convolutional layers that apply small filters across the input to detect patterns, edges, and textures. These filters slide over the entire input, performing element-wise multiplications and aggregating results to form feature maps. In our analysis, we also demonstrated that the DL-based framework has the capability to map antenna temperature with reduced reference and ND information. This will help in increasing spatial and temporal resolution through more frequent antenna temperature measurements. The large dataset from SMAP has enabled us to learn a new model for predicting antenna temperature. First preprocessing of the data for the input of DL is discussed. Next design and training of the DL architecture is discussed. In the later sections, the evaluation and performance metrics are addressed. Various train/test scenarios are discussed, accompanied by suitable performance metrics to elucidate the estimation performance.

## A. Data Prepocessing

Before going into the model, preprocessing the data is critical for DL-based frameworks. Meaningful features play a crucial

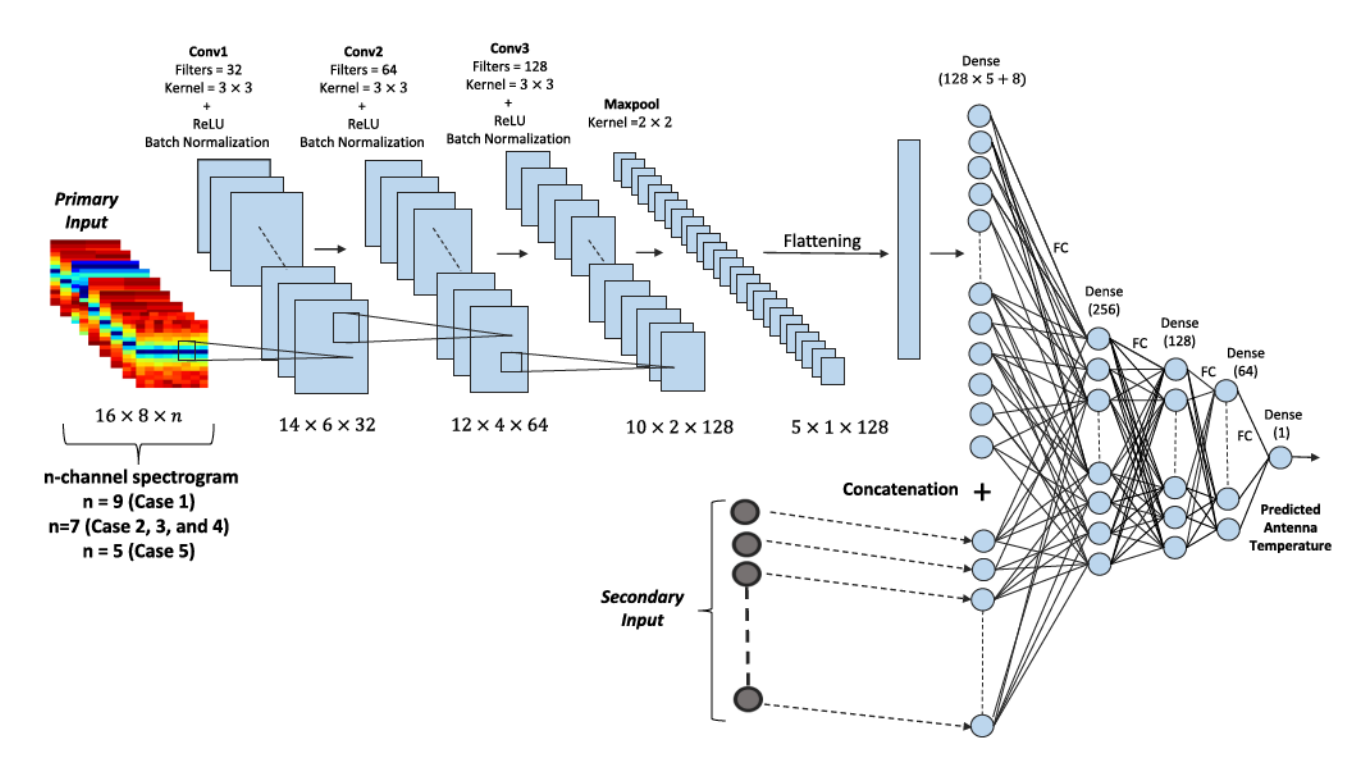


Fig. 5. DL architecture to predict antenna temperature.

role in the convergence of models as filters and parameters primarily aim to establish a relationship between input features and output labels. Utilizing SMAP level 1B quality flags, footprints that are not contaminated by RFI are identified and used in this study. SMAP quality flags contain nine different algorithms to label a particular pixel whether it has RFI or not [16], [17], [24]. The distribution of the input samples is inspected to find possible outliers in the dataset. The performance of DL-based frameworks can be negatively impacted by the presence of outliers [35]. RFI quality flags primarily focus on the distribution of the dataset so there were no possible outliers in the input samples. Subsequently, features that exhibit a consistent value across all samples are identified. Static features do not contribute new information to the model, and as the system iterates, they are eventually disregarded [36]. During conventional radiometer calibration, features, such as loss, in radome are considered. However, this particular feature maintains a constant value across all samples and is not taken into consideration in this study. Table I displays both the total available samples and those effectively employed in DL-based calibration.

## B. Design of the DL Architecture

The proposed DL framework illustrated in Fig. 5 comprises three main components: convolutional layers, concatenation layers, and densely connected layers. The convolutional layers are responsible for extracting features from n-channel spectrograms. After the convolutional layers, the features are flattened and combined with other secondary feature inputs through concatenation. To map the concatenated features to the radiometer

antenna temperature, three layers of fully connected neural networks are utilized.

2-D spectrograms consisting of information about the observation, reference, ND, and phases are the primary input to the CNN-based DL framework. To analyze the dependence on reference points, the same framework has been trained and tested under 5 different train/test cases. This shows the flexibility of a DL-based model over conventional forward modeling techniques. Three convolutional layers consisting of 32, 64, and 128 filters are utilized to extract meaningful features from the input spectrograms. The filters in the convolutional layer are  $3 \times 3$ kernels without any padding. Each convolutional layer is accompanied by ReLU activation and batch normalization layer. ReLU activation helps in introducing nonlinearity in the computation and introduces a threshold or cutoff point for the output of a neuron [37]. Batch normalization is a technique that normalizes the activations within a mini-batch of training examples. It works by scaling and shifting the activations on a per-feature basis to achieve zero mean and unit variance. This normalization process is beneficial as it reduces the internal covariate shift, which refers to the change in the distribution of layer activations during training. By maintaining stable distributions, batch normalization enables subsequent layers to learn more efficiently and promotes faster convergence of the network [38]. As features are not normalized before going into the model, batch normalization helps in convergence by reducing the need for careful initialization. A total of 640 (i.e.,  $128 \times 5 = 640$ ) features are extracted from the convolutional layers and they are flattened to combine with secondary features. After combining, they go through three consecutive fully connected layers with 256, 128, and 64 neurons. These dense layers are propagated

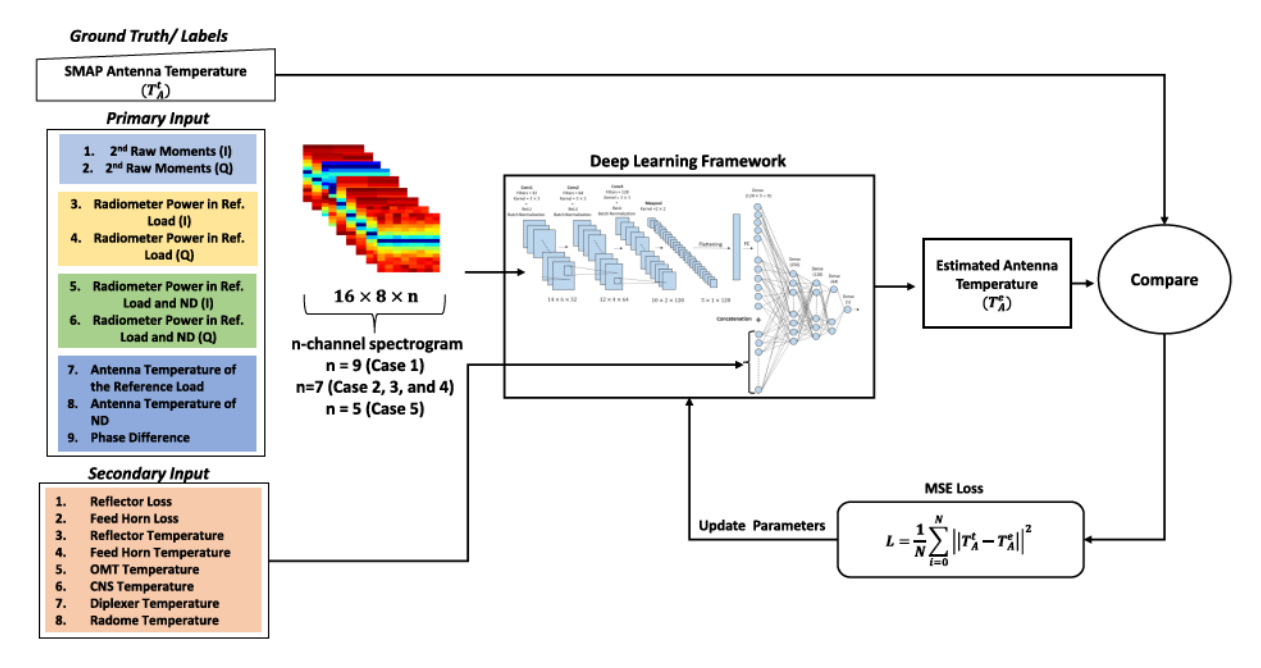


Fig. 6. Training of DL-based architecture to estimate antenna temperature.

with the ReLU activation function. The last layer of this network consists of a single neuron with a linear activation function to produce the final output.

## C. Training the DL Architecture

Fig. 6 illustrates the flowchart outlining the training process of the proposed DL architecture. The model is trained and tested with five different training cases mentioned in Section II-E. The DL-based model discussed in the previous section estimates antenna temperature and the only distinction lies in the input layers for different training scenarios. The secondary features concatenate with the extracted features from the CNN layer by fully connected layers to map the final antenna temperature in all cases.

The SMAP antenna temperature for a particular footprint is considered as ground truth for this study. To achieve global coverage with varying temporal and spatial resolutions, we utilized data from the Earth observation satellite service SMAP. To update the parameters of the DL model, it is backpropagated with a mean squared error (mse) loss function given as

$$L = \frac{1}{N} \sum_{i=1}^{N} \left| \left| T_A^t - T_A^e \right| \right|^2 \tag{1}$$

where  $T_A^t$  is ground truth antenna temperature extracted from SMAP level 1B data products and  $T_A^e$  is output from the DL-based calibration model. N is the total number of samples used in one iteration. This loss function is not polarization-specific and can be utilized for different polarizations. The model has been trained with 128 batch sizes and 40 epochs. To minimize the loss function Adam optimizer has been used in this study [39]. It incorporates adaptive learning rates for each parameter, adjusting them based on the gradients and the moving average of past gradients. In order to ensure the development of a model that

generalizes well and avoids overfitting the training data, several techniques have been incorporated. These include the use of learning rate schedulers [40] and early stopping [41], [42]. The learning rate plays a crucial role in determining the magnitude of changes made to the model weights during the training process, based on the predicted error. Setting the learning rate too small can result in a lengthy training process while setting it too large can lead to unstable training and failure to converge. To address this, a learning rate scheduler has been implemented in this study, specifically an exponential learning rate scheduler. This approach involves gradually decreasing the learning rate after each iteration of the model. Exponential learning rate decay involves initializing the learning rate to 0.001 and progressively reducing it after each epoch. By doing so, the model can refine its parameters more effectively over time, leading to improved convergence and potentially better generalization. The combination of exponential learning rate decay and early stopping contributes to a more robust and reliable training process, enabling the model to strike a balance between fitting the training data and generalizing well to unseen data.

## D. Evaluation and Performance Metrics

CV is a fundamental procedure employed for assessing the generalization capability and efficacy of DL models. It finds wide application in situations where the primary objective is prediction, regression, or classification, enabling the evaluation of a model's performance in real-world scenarios. This study employs three CV techniques, namely: 1) train-test split, 2) K-fold, and 3) time-based analysis. These techniques are employed to assess the generalization capability in five distinct cases, encompassing various combinations of different FG detailed in Section II-E.

In train-test split CV, the dataset is partitioned into training and testing sets randomly, with an 80% portion allocated for training and the remaining 20% for testing. The selection of training and testing samples is conducted randomly, encompassing the entirety of the dataset across various geographical regions and temporal intervals. K-fold CV (for this study K = 5) utilized in this study partitions the dataset into k subsets of equal size. It iteratively selects one subset as the testing set and the remaining K-1 subsets as the training set. The model is trained and evaluated K times, with a different subset serving as the testing set in each iteration. Performance metrics are recorded for each iteration, and the average of these results provides a more reliable estimate of the model's performance. This technique reduces bias and variability compared with a single train-test split. K-fold enhances performance assessment by considering multiple data partitions, facilitating model generalization, and aiding in model selection and hyperparameter tuning.

In addition to employing traditional CV techniques, this study incorporates a time-based CV approach by dividing the training and testing datasets based on different time spans. Specifically, samples from each year spanning 2017–2022 are considered. The DL framework is trained using data from 2017 and subsequently tested using data from 2018 to 2022. In another analysis, the DL-based calibrator is trained with samples from [2017, 2018] and tested with data from 2019 to 2022. This evaluation methodology enables the examination of the radiometer's characteristics over time and determines whether features learned from a specific period can be effectively used to model the calibration process of future time periods. The experimental results contribute to a comprehensive understanding of the radiometer's overall characteristics and the time-dependent effects of individual features.

 $R^2$  or the coefficient of determination is a widely utilized performance metric in regression analysis. It quantifies the extent to which independent variables explain the variability in the dependent variable. With values ranging from 0 to 1, an  $R^2$  value of 0 denotes the lack of explanatory power, while a value of 1 signifies a perfect fit of the independent variables to the dependent variable. Thus,  $R^2$  serves as a measure of the goodness of fit for a regression model, indicating a better fit with higher values.  $R^2$  can be calculated as

$$R^{2} = 1 - \frac{\sum_{i=1}^{N} (T_{A}^{t} - T_{A}^{e})}{\sum_{i=1}^{N} (T_{A}^{t} - T_{A}^{M})^{2}}$$
(2)

where N is the number of observations in the dataset.  $T_A^t$  represents the true values of antenna temperature.  $T_A^e$  represents the estimated values of the antenna temperature with DL.  $T_A^M$  represents the mean of the true values of the antenna temperature. Nonetheless, it should be noted that  $\mathbf{R}^2$  alone cannot determine the overall quality or validity of a model, as it can be influenced by factors, such as the number of predictors, model complexity, and the presence of outliers. Therefore, it is often used in conjunction with other evaluation metrics for a comprehensive assessment of regression model performance. The root mean square error (RMSE) is a widely employed metric in regression analysis to assess the accuracy and performance of regression

TABLE III
PERFORMANCE METRICS OF DL-BASED CALIBRATOR WITH TRAIN-TEST SPLIT
AND K-FOLD

Validation	Training	Land	i	Land and Water		
Techniques	Scenarios	RMSE (K)	R <sup>2</sup>	RMSE (K)	$\mathbb{R}^2$	
	Case 1	0.24	0.9998	0.29	0.9997	
	Case 2	0.42	0.9994	0.40	0.9995	
Train-Test Split	Case 3	0.43	0.9994	0.37	0.9996	
SPA.	Case 4	0.35	0.9996	0.33	0.9996	
	Case 5	0.67	0.9991	0.45	0.9993	
	Case 1	0.27	0.9997	0.31	0.9997	
	Case 2	0.45	0.9993	0.41	0.9994	
K-Fold	Case 3	0.47	0.9992	0.40	0.9994	
	Case 4	0.37	0.9996	0.36	0.9996	
	Case 5	0.72	0.9990	0.51	0.9992	

models. This metric quantifies the average magnitude of the residuals or prediction errors generated by the model. RMSE is given as

$$RMSE = \sqrt{\frac{1}{N} \sum_{i=1}^{N} ||T_A^t - T_A^e||^2}$$
 (3)

where  $T_A^t$  is ground truth antenna temperature and  $T_A^e$  is output from the DL-based calibration model. N is the total number of samples. It is crucial to note that the performance metrics presented in the subsequent Results section were computed on a testing dataset that was previously unseen by the model.

# IV. RESULTS

In this section, we present a comprehensive performance analysis of radiometer antenna temperature estimation utilizing the DL-based framework. In Section IV-A, performance with train-test split and K-fold has been demonstrated with five different training scenarios. Dependency on data is presented in Section IV-B. Computational complexity is explained in Section IV-C. Comparison between existing ANN and proposed DL approach has been illustrated in Section IV-D. Finally, time-based CV is detailed in Section IV-E.

## A. Overall Performance of DL-Based Calibrator

The overall performance with a DL-based calibrator predicting antenna temperature is illustrated in Table III. This analysis is performed with two validation techniques—train-test split and K-fold. Both V-pol and H-pol show very similar performance with DL-based calibration and throughout the rest of this article, all the performance metrics are shown in terms of V-pol. A particular validation technique has five different training and testing scenarios. The dataset comprises samples obtained from both land and land—water combinations in each case. In the train-test split CV approach, Case 1 demonstrates superior performance by achieving the lowest RMSE values for both land and land—water sample combinations, with RMSE values of 0.24 and 0.29, respectively. Furthermore, Case 1 exhibits high levels of predictive accuracy, as indicated by the high

R-squared values of 0.9998 and 0.9997 for land and land-water combinations, respectively. The findings of this case indicate that a DL-based calibrator exhibits comparable efficacy in estimating antenna temperature for radiometers. Performance with land and land-water mix samples shows that ground-only samples are enough and demonstrate no additional biases to achieve good performance in calibration. It is crucial to bear in mind that in Case 1, DL employs an equivalent number of features as a conventional radiometer utilizes for calibration. In Case 2, DL shows RMSE of 0.42 and 0.40 with land and land-water combination, respectively. R-squared value of 0.9994 and 0.9995 shows a high correlation between the ground truth and the predicted value. In Case 2, power information of reference load is not utilized during training and testing. The only information that is available from the reference is its physical temperature. The low RMSE value shows that DL has the capability to estimate antenna temperature with less reference information. The nonlinear modeling capabilities of DL enable it to capture complex relationships and patterns within the available FG that may be challenging for traditional linear calibration models to capture. Case 3 exhibits a similar performance as Case 2. The observed performance enhancement in Case 3 suggests that the combination of the reference plus ND power provides a richer set of feature information that is closely associated with the antenna temperature. Case 4 shows better performance than both Case 2 and Case 3 with RMSE of 0.35 and 0.37, respectively, for land and land-water combination. Case 4 utilizes a single packet of power information from both reference and reference plus ND. This scenario helps to extract critical features from both of these calibration units which has an impact on overall performance. In Case 5, performance deteriorates from other training scenarios. This is because no reference and reference plus ND power features have been used during the training and testing of the model. Important considerations can be-DL-based calibrator has RMSE of 0.67 K and 0.45 K with land and land-water combination which is still less than the SMAP radiometer uncertainty that is 1.3 K. Training and testing with both land-water mix data provide lower RMSE comparing the cases with training and testing over land only. This might be due to the fact that the land-water mix has more samples with diverse feature information. Another reason can be that samples from the water provide features that have lower antenna temperatures (i.e., 70–110 K) compared with the ground-based samples. A higher dynamic temperature range in the land–water mix helps the DL-based calibrator to learn the important feature information compared with ground-based samples. Fig. 7 shows a comparison with the Case 5 training scenario. The same set of observations are considered for this analysis and it can be seen that land-water mixed samples provide better performance over land-only samples. To understand the robustness and unbiased estimation of the model, performance with K-fold is depicted in Table III. The observed performance exhibits a similar pattern to that of the train-test split technique, providing evidence that the DL-based calibrator demonstrates resilience against data variability and overfitting. Case 1 shows the best performance among the training scenarios with RMSE of 0.27 K and 0.31 K for both land and land-water combinations, respectively. However,

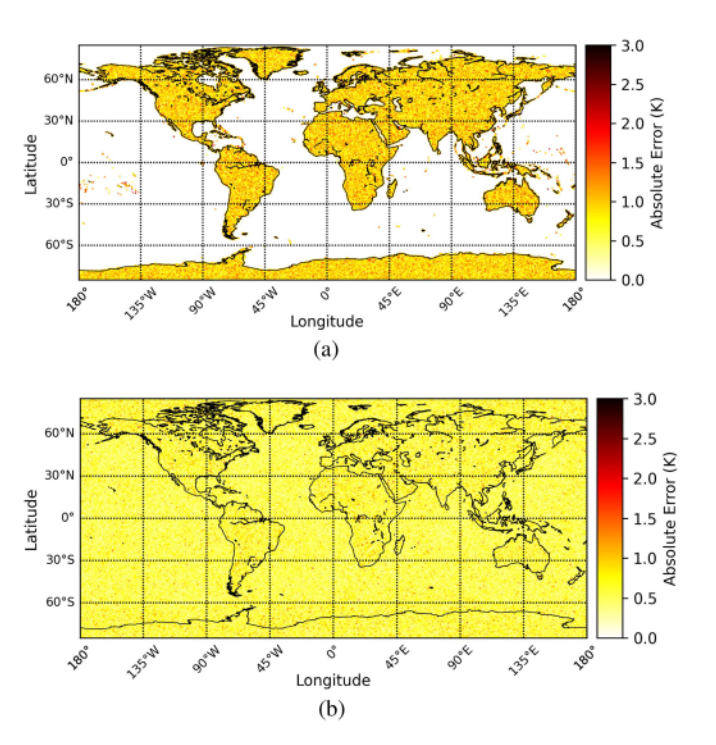


Fig. 7. Absolute error with Case 5 training/testing scenario with (a) land and (b) land-water mix.

reduced reference information in Cases 2–5 shows significantly low RMSE and high R-squared performance. Choosing the correct training scenarios lies within the specification of the radiometer. If the error budgeting process for a spaceborne radiometer necessitates high radiometric resolution and reduced radiometric uncertainty, the calibration training scenarios employed in Case 1 and Case 4 exhibit promising characteristics and can be considered as ideal options. To enhance the reliability of data products within a footprint by incorporating a greater number of scene observations, the utilization of Case 2, Case 3, and Case 5 calibration training scenarios could prove to be effective strategies.

Fig. 8 illustrates the spatial distribution of the antenna temperature, showcasing a comparison between the ground truth and predicted values. This analysis will be critical to understanding any spatial discrepancy with the predicted antenna temperature. Fig. 8(a) shows ground truth antenna temperature zoomed over a certain location—for this study, USA is chosen. Fig. 8(b) shows the antenna temperature profile predicted by the DL-based calibrator. The spatially distributed profiles of the antenna temperature exhibit a high degree of similarity, indicating that the DL-based calibrator demonstrates negligible spatial variability within the sampled data. Fig. 8(c) helps to understand the absolute error between ground truth and predicted antenna temperature. The results demonstrate that the absolute error of each sample remains within the range of 0.2 K. This analysis is based on the Case 4 training scenario. Fig. 9 will help to understand the absolute error with different training scenarios proposed in this study. In each case, spatially distributed absolute error is plotted. The RMSE with train/test split between 5 cases is 0.24, 0.42, 0.43, 0.35, and 0.67 K, respectively. Case 1

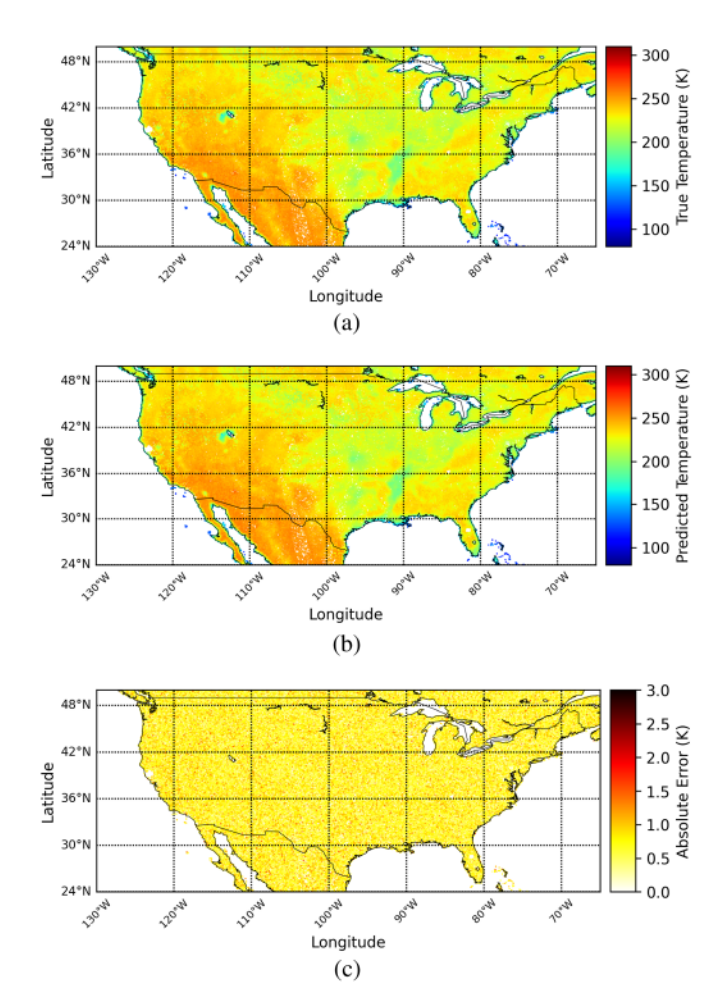


Fig. 8. Comparison of antenna temperature between ground truth and predicted antenna temperature over USA with Case 4 training scenario. (a) Ground truth antenna temperature from SMAP, (b) predicted antenna temperature with DL, and (c) absolute error for each footprint between ground truth and predicted value.

[see Fig. 9(a)] and Case 4 [see Fig. 9(d)] provide the best performance because of the availability of both reference and ND power information. Case 2 [see Fig. 9(b)] and Case 3 [see Fig. 9(c)] performance deteriorates because of reduced reference information. With land-only samples, it becomes challenging for the DL-based framework to estimate antenna temperature with no reference power information evident in the Case 5 scenario shown in Fig. 9(e).

In Fig. 10, we examine the error probability density graph for various cases. Notably, Case 1 and Case 4 exhibit higher density with lower error values, indicating favorable performance. However, Case 2 and Case 3 experience performance deterioration due to missing reference voltage values, yet they still maintain error values within a range of 1.3 K. Furthermore, Case 5 demonstrates higher error values due to the absence of both reference and ND information. Despite this, our findings suggest that even with reduced reference information, it is possible to leverage DL-based calibration techniques to predict antenna temperature. These results underscore the significance of reference information in enhancing performance. However, they also

highlight the potential for utilizing limited reference information in DL-based calibrators to achieve accurate predictions.

During the training of a DL model, it is crucial to assess whether the model is exhibiting signs of overfitting or underfitting. Overfitting occurs when a model performs well on the training data but fails to generalize effectively to testing samples. Underfitting, on the other hand, refers to a model's inability to perform adequately on both the training and testing data. Finding the optimal balance in DL, known as a good fit, is of utmost importance. A good fit is achieved when both the training and test loss consistently decrease after each epoch and eventually converge to a low loss level, as illustrated in Fig 11. This is plotted for the Case 4 training scenario with land-based samples and other training scenarios show similar behavior.

#### B. Data Dependency

This study has developed a supervised DL framework to predict antenna temperature for the SMAP radiometer. The data distribution consists of samples from various spatial and temporal distributions. This section will provide a quantitative analysis in terms of choosing the amount of data required to predict antenna temperature. For each case, the test dataset is kept fixed and the training dataset is changed from 5% to 80%. RMSE performance for five different cases with respect to training size is shown in Fig. 12. It also shows a fixed SMAP radiometer uncertainty line of 1.3 K [15], [27]. If RMSE is under that region for a particular training scheme, it might be considered acceptable. For all cases, RMSE is decreasing with increasing training sizes. In the previous analysis, the overall dataset is randomly divided into 80% training and 20% testing. However, analysis shows that during Case 1 and Case 4 RMSE is under the uncertainty range with 25% of the training dataset. Cases 2 and 3 require a higher number of training samples (around 40%) to get the error under that range. Case 5 needs around 60% of the total samples to achieve similar performance. Cases 1 and 4 contain one packet reference and reference plus ND power features that help in quick convergence. Because of the absence related to reference information Cases 2 and 3 require a higher number of training samples. Case 5 requires more data to achieve this performance as it does not utilize any power features from reference and reference plus ND. This analysis proves it requires more training data for DL-based calibrators if there is less reference information available. After 60% Cases 1-4 mostly converges to the same level. Case 5 converges to a little higher level after 70% of training data but still below the 1.3 K range. This analysis overall proves that the DL-based calibrator shows satisfactory performance even with reduced reference information and training

RMSE will indicate how close we obtain to current SMAP antenna temperature values. But to understand how well the DL-based calibration algorithm performs over known sources in comparison with the SMAP values we provided a measure of the distribution of the calibrated values with the help of standard deviation (STD). STD is calculated over a particular region in the Amazon rain forest, Antarctica Dome C, and the North Atlantic Ocean. Historical data illustrates the presence of homogeneity

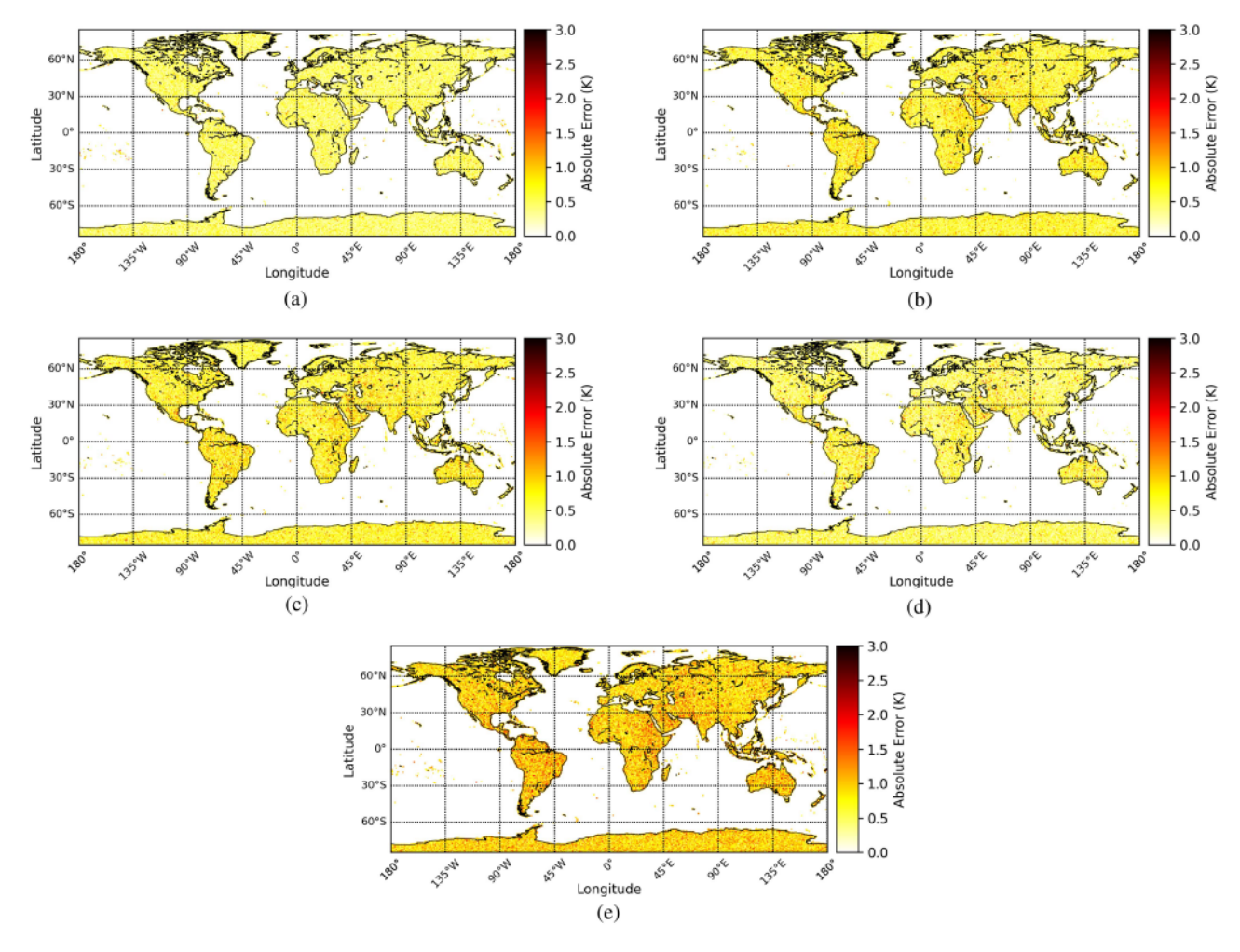


Fig. 9. Spatially distributed absolute error between ground truth SMAP antenna temperature and predicted antenna temperature with DL for (a) case 1, (b) case 2, (c) case 3, (d) case 4, and (e) case 5.

within the Amazon Basin and Dome C region, making it a valuable asset for satellite radiometer calibration [43], [44], [45]. Nevertheless, STD may be influenced by the day of the year, the specific time on a given date, and the geographic area within the region [46]. Fig. 13 shows STD with different time intervals for SMAP and DL in the Amazon, Antarctica Dome C, and North Atlantic Ocean region. As the time interval increases, the STD also shows an upward trend, reflecting the changing weather conditions and their consequential impact. It also shows that STD obtained with the DL-based calibrator is always lower than SMAP's conventional calibration technique. This observation underscores that the fluctuations in antenna temperature estimates, when utilizing the DL-based calibrator, are notably smaller compared with the SMAP's conventional calibration method. It is plausible to assert that the DL approach yields estimates that closely align with the expected antenna temperature readings, particularly when one anticipates a stable temperature reading during the brief interval of an antenna scan cycle. This propensity may be attributed to the intricate, nonlinear structure inherent in DL, which has the capacity to resolve the intricate radiometer characteristics. Nonetheless, it is essential to exercise caution when asserting that the DL calibrator results in lower

radiometric resolution compared to the conventional technique, given the inherent limitations in system information. Although the DL calibrator yields estimates much closer to the desired radiometer output than its conventional counterpart, a more comprehensive evaluation could be facilitated through thermal chamber experiments that include controlled target temperature observations of the radiometer. To determine whether there exists a significant bias in the antenna temperature estimates between SMAP and the DL-based calibrator, the difference between mean values is computed. The bias between the mean of SMAP and DL-based calibrator in Amazon, Dome C, and North Atlantic Ocean are 0.44, 0.35, and -0.04 K, respectively. Lower bias and STD values demonstrate higher accuracy and lower uncertainty for the performance of the DL-based calibrator.

## C. Computational Complexity

One important aspect of data-driven models is computational complexity. The model required 28.72 h training and 0.23 h testing time for land-based samples with an 80–20 split. For landwater mix samples training time increased to 49.53 h and testing

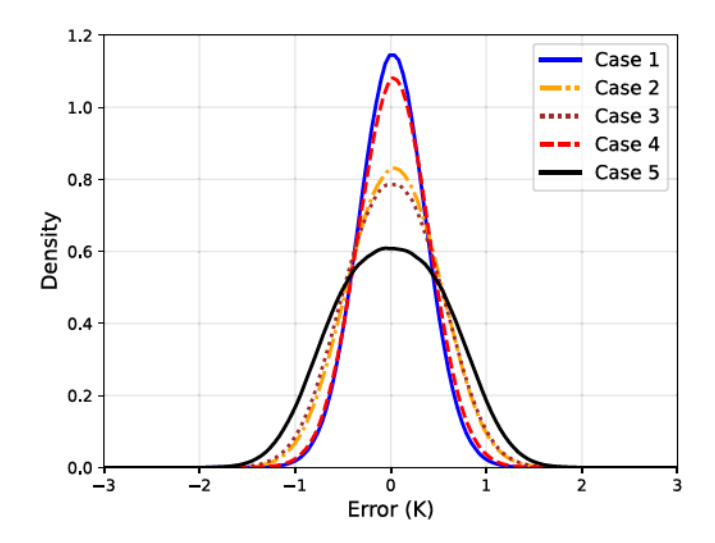


Fig. 10. Density variation of ground truth and predicted antenna temperature difference (error) in different cases.

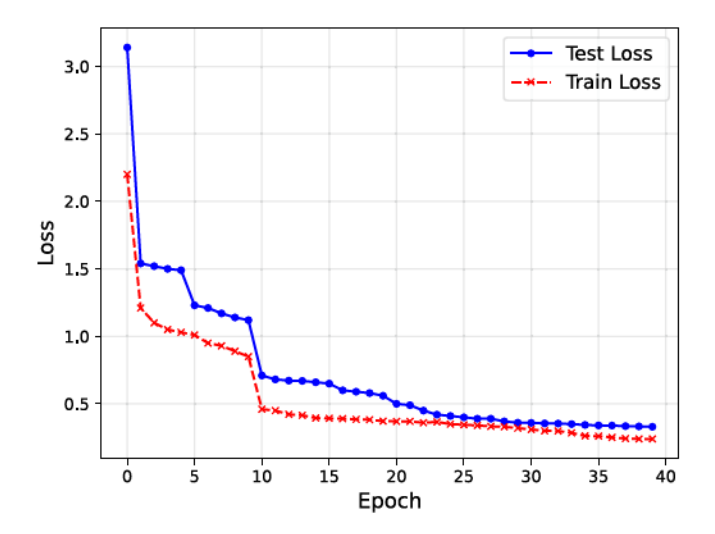


Fig. 11. Model loss on training and testing dataset.

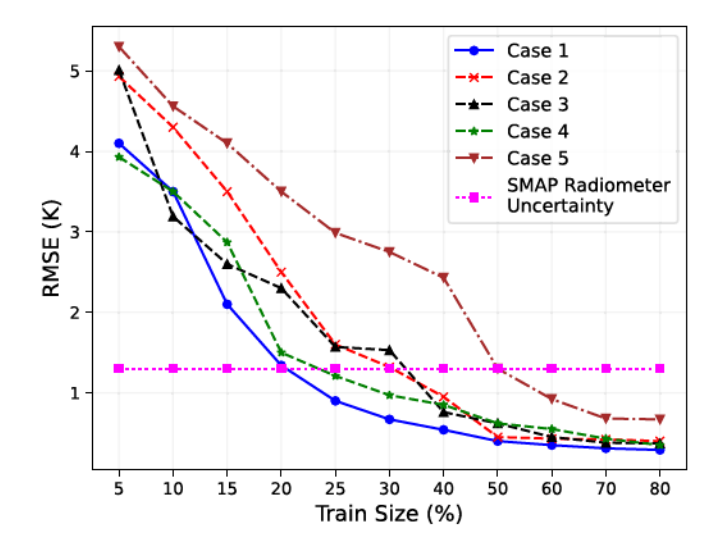


Fig. 12. Comparing RMSE errors of various training scenarios with SMAP radiometer uncertainty.

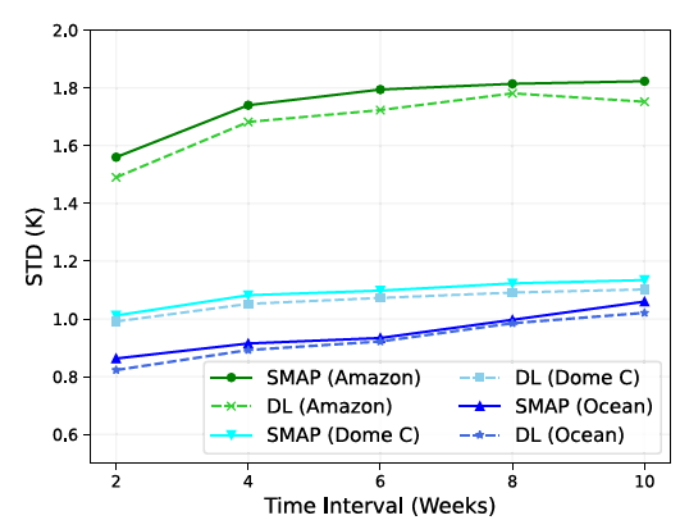


Fig. 13. STD of measured antenna temperature with SMAP and DL-based calibrator (Case 4) over a specific region in Amazon rain forest, Antarctica Dome C, and North Atlantic Ocean with different time intervals.

time 0.45 h. For K-fold training time increases to 41.3 h for land-based samples and 62.5 h for land-water mix samples. After saving the model state by completing the training and validation, it requires around 0.06 s to predict antenna temperature within a footprint. Future studies aim to optimize the model even further and develop an onboard calibration inside the radiometer digital back-end unit. The DL model is developed using the Pytorch Python interface [47], [48]. It is trained and tested on a machine with Intel(R) Xeon(R) Platinum 8260 CPU @ 2.40 GHz, 512 GB memory, and NVIDIA TITAN RTX GPU. A total of 302,337 parameters are used to develop the DL-based calibrator.

## D. Comparison Between ANN and DL-Based Calibrator

In this section, a comparison between DL and ANN-based calibrators will be demonstrated. This analysis will help to understand if the CNN-based DL framework is able to extract crucial information from the two-dimensional spectral features of the radiometer. ANN utilized in this study is directly taken from this [12]. This is based on a multilayer perceptron feedforward neural network model with three hidden layers. The main difference between this study's CNN-based calibrator and ANN is that CNN is capable of extracting meaningful features from 2-D input directly, whereas ANN utilizes single-value features (averaging the power over 2-D domain) to estimate antenna temperature.

Table IV gives the performance comparison between ANN and DL with five different training scenarios along with land and land-water mix samples. Performance metrics show that with the Case 1 training scenario both DL and ANN give a similar performance with RMSE of 0.24 K and 0.38 K respectively with land-only samples along with RMSE of 0.29 and 0.37 K with land-water mix samples. Across Cases 2–5, the performance of the ANN calibrator exhibits a notable decrease in comparison to its DL-based calibrator. It shows that reduced reference and ND features have a significant impact on ANN-based calibrators

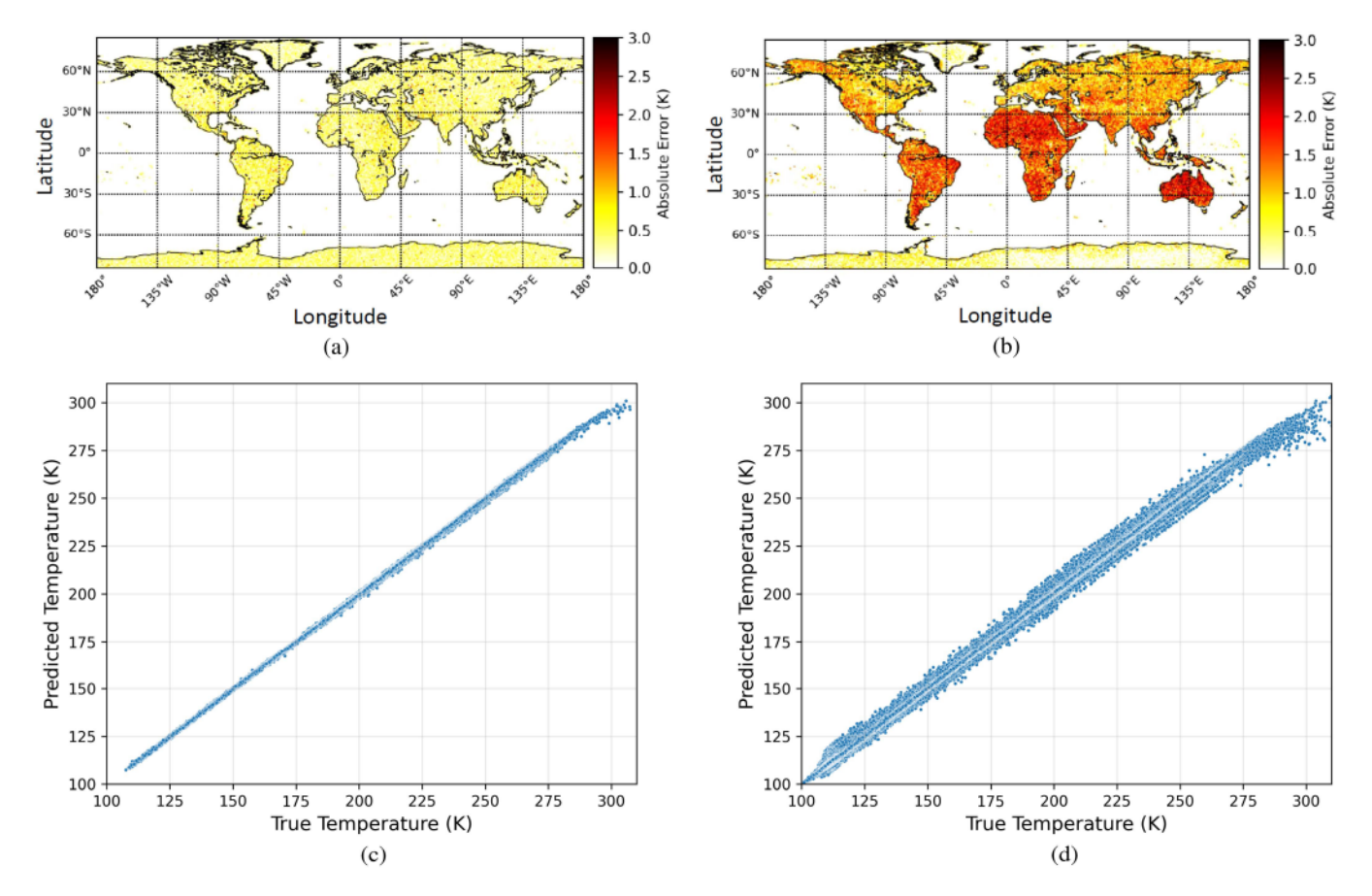


Fig. 14. Performance comparison in terms of absolute error between (a) DL-based calibrator and (b) ANN-based calibrator. Correlation between true antenna temperature and predicted antenna temperature with (c) DL-based calibrator and (d) ANN-based calibrator. This analysis is conducted with Case 4 training scenario.

TABLE IV
PERFORMANCE COMPARISON BETWEEN DL AND ANN-BASED CALIBRATOR

Calibrator Techniques	Training	Land	1	Land and Water			
	Scenarios	RMSE (K)	R <sup>2</sup>	RMSE (K)	$\mathbb{R}^2$		
DL	Case 1	0.24	0.9998	0.29	0.9997		
	Case 2	0.42	0.9994	0.40	0.9995		
	Case 3	0.43	0.9994	0.37	0.9996		
	Case 4	0.35	0.9996	0.33	0.9996		
	Case 5	0.67	0.9991	0.45	0.9993		
ANN	Case 1	0.38	0.9994	0.37	0.9994		
	Case 2	1.56	0.9942	1.54	0.9944		
	Case 3	1.63	0.9939	1.59	0.9941		
	Case 4	1.32	0.9951	1.27	0.9952		
	Case 5	1.73	0.9935	1.62	0.9937		

compared with DL. Fig. 14(a) and (b) demonstrate the performance comparison in terms of absolute error between the DL-based calibrator and ANN-based calibrator with the Case 4 training scenario. RMSE between DL and ANN-based calibrator is 0.35 and 1.32 K, respectively. Fig. 14(c) and (d) shows the correlation between true antenna temperature and predicted antenna temperature of DL and ANN-based calibrators, respectively. R<sup>2</sup> between them is 0.9996 and 0.9951, respectively. The

analysis of performance metrics using land—water mix samples demonstrates comparable results, with a slight improvement in performance compared with land-only samples. The DL-based calibrator demonstrates superior performance in terms of both 2-D spectral features and the utilization of reduced reference information.

## E. Time-Based Analysis

This section will provide results of the DL-based calibrator when it is trained with samples from a particular time frame and tested in another. During this CV we have analyzed two different training scenarios. 1) Trained the model with samples from 2017 and tested it with samples from 2018 to 2022. 2) Trained the model with samples from 2017 to 2018 and tested from 2019 to 2022. Both of these analyses will be critical to understanding if samples from a particular time frame are enough to predict antenna temperature in a future time frame. For example, testing a model trained over only 2017 data in 2022 will be evaluating the validity of the DL model after 5 years.

Tables V and VI illustrate the performance when the model is trained with samples from 2017 and [2017, 2018], respectively. The performance table is divided into five different training scenarios with land and land—water mix samples. The RMSE of each year's sample is given in each row. Performance metrics in

Training Scenarios	Land				Land and Water					
Year Wise RMSE (K)	Case 1	Case 2	Case 3	Case 4	Case 5	Case 1	Case 2	Case 3	Case 4	Case 5
2018	0.29	0.44	0.45	0.37	0.71	0.31	0.41	0.39	0.36	0.47
2019	0.32	0.47	0.49	0.39	0.75	0.32	0.43	0.42	0.38	0.52
2020	0.34	0.51	0.52	0.41	0.95	0.33	0.44	0.45	0.41	0.56
2021	0.37	0.56	0.55	0.44	1.11	0.37	0.47	0.49	0.42	0.61
2022	0.41	0.55	0.57	0.47	1.32	0.39	0.48	0.51	0.45	0.65

TABLE V
PERFORMANCE METRICS TIME-BASED ANALYSIS [TRAINED WITH SAMPLES FROM 2017]

TABLE VI
PERFORMANCE METRICS TIME-BASED ANALYSIS [TRAINED WITH SAMPLES FROM 2017 AND 2018]

Training Scenario	Land				Land and Water					
Year Wise RMSE (K)	Case 1	Case 2	Case 3	Case 4	Case 5	Case 1	Case 2	Case 3	Case 4	Case 5
2019	0.31	0.44	0.48	0.37	0.73	0.33	0.42	0.41	0.36	0.49
2020	0.33	0.51	0.50	0.41	0.89	0.32	0.43	0.44	0.40	0.54
2021	0.36	0.55	0.53	0.43	1.05	0.35	0.46	0.47	0.43	0.59
2022	0.40	0.58	0.56	0.46	1.21	0.38	0.48	0.49	0.45	0.63

both of these tables show that if the duration between training and testing samples increases (i.e., train with 2017 test with 2022), performance will deteriorate. This could be because during the long lapse between training and testing time-frames, radiometer instrument characteristics might have changed or the receiver parameters have drifted. Comparing the performance with 2022 samples for both of the time-based CV, it is evident that when the model performs better when it is trained with 2017-2018 samples than the 2017 samples. The number of samples might play a crucial role in that result. The model might also perform better because there is less time-lapse between training and testing with 2017–2018 samples. A sharp decline in performance is noticeable with Case 5 in the land-based samples for both timebased CV, whereas land-water mix samples for Case 5 have less drift in RMSE over the years. Extracted features from land-water mix samples might compensate for less reference information in this particular training scheme. During the development of a DL-based calibrator, this might be important information for consideration.

Fig. 15 will help to understand the spatial variability of the samples in terms of the absolute error calculated for each footprint. This figure shows the absolute difference between the ground truth and predicted value with years from (a) 2018, (b) 2019, (c) 2020, (d) 2021, and (e) 2021. The initial training of the model is performed using samples from the 2017 land—water mix dataset with Case 5. During shorter time lapses between training and testing dataset, there is less absolute error within the samples evident in Fig. 15(a)—(c). However, as the duration arises between training and testing dataset there are differences between ground truth and predicted value. Fig. 15(d) shows some sparse hot spots with absolute error values and not a fixed spatial location that contains those errors. But in Fig. 15(e) there is a high absolute error in Africa (latitude 34.5°S and longitude

 $-8^{\circ}$ W). However, it is important to consider that the highest RMSE within those years (illustrated in Table V—land and water—Case 5) is 0.65 K. This analysis is portrayed with Case 5 training scenarios but other cases have better performance in terms of RMSE and spatial variability. This is because samples contain some sort of reference and ND power information from the radiometer.

#### V. DISCUSSION AND FUTURE WORK

This study has provided empirical evidence that DL can be effectively employed for radiometer calibration, requiring reduced reference information while utilizing 2-D antenna counts partitioned into time and frequency subbands. The developed calibration framework has been validated with different strategies, such as K-Fold and time-based analysis, to understand the robustness and generalization capability. The data-driven technique has been further trained and tested with land-only and land-water mix samples. The findings indicate that the utilization of a composite mixture of land-water samples contributes to the development of an augmented dynamic range, thereby facilitating performance improvement. A comparative analysis has been conducted between the proposed calibration technique and a pre-existing calibration framework based on ANN. The incorporation of 2-D spectral features in this study's DL-based calibrator has demonstrated enhanced performance with reduced reference information when compared with the ANN-based calibrator. Lower RMSE and high R<sup>2</sup> values with reduced reference information show the capability of DL to extract valuable information from the input features. Both V-pol and H-pol have exhibited similar performance under DL-based calibration. Future studies may extend DL-based calibration to

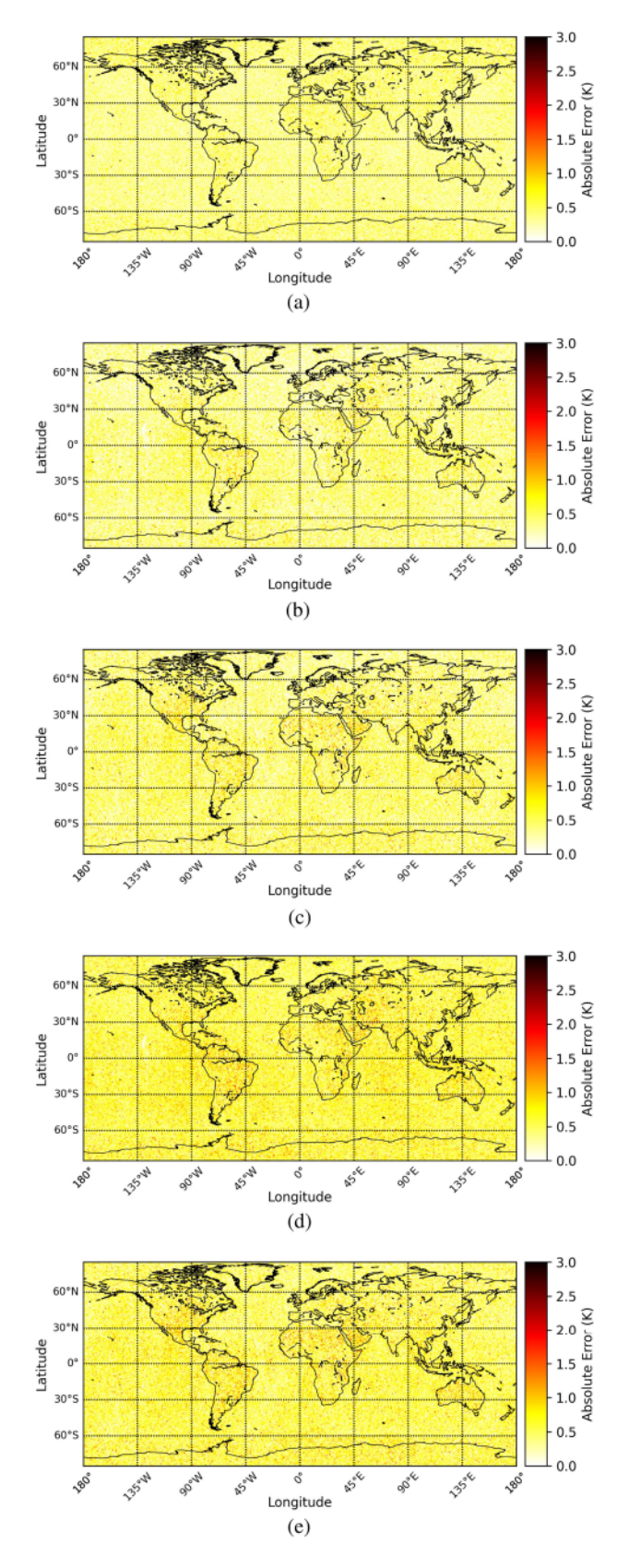


Fig. 15. Spatially distributed absolute error (K) with time-based CV and training Case 5. The DL model is trained with 2017 samples and tested with (a) 2018, (b) 2019, (c) 2020, (d) 2021, and (e) 2022 samples.

include the third and fourth Stokes antenna temperatures, with a focus on careful input feature selection.

This study could be an attractive alternative to the overall calibration unit. Since we are using calibration outputs of SMAP as ground truth to train the model, our predictions can only be a proxy to SMAP's algorithm. However, this DL-based calibration procedure has the capability to directly compare with the conventional radiometer outputs by conducting controlled experiments in anechoic and environmental chambers. In future studies, the proposed calibration framework will be trained and tested with our developed radiometer [49]. This DL-based calibrator will serve as a crucial component within a data-driven microwave radiometer framework. The framework will encompass an already developed RFI detection and mitigation unit, followed by the DL-based calibrator [50]. The calibration unit proposed in this study exhibits potential for application in wideband radiometers, particularly due to its ability to effectively utilize time-frequency 2-D data that was not directly employed in the calibration process previously. Different training schemes discussed in this article can be useful to identify a proper DL-based calibrator that meets the requirements.

Supervised DL-based techniques might require a substantial amount of data to learn the complex relationship between inputs and outputs which might be challenging and expensive. However, DL does not require an exhaustive dataset that covers every possible input-output scenario. Instead, a subset of measurements within a defined range is adequate for initializing DL-based models, obviating the need for exhaustive data inclusion. This diversity helps the model generalize and learn the underlying patterns within the data, which is evident in this study's land and land-water combination results. Instruments undergo rigorous thermal and vacuum chamber testing, generating millions of data points. These data sets are ample for constructing a model and training a system to replicate a radiometer's behavior. However, it is crucial to take careful consideration in addressing the difference between on-ground and on-orbit environmental differences. After launch, raw data samples collected from vicarious sources or other calibration sources can be used to tune the DL-based calibration of the instrument during on-orbit operation. This adjustment accounts for on-orbit effects, nonstationary instrument changes, such as aging and orbital variations. Like traditional calibration methods, DL-based calibration models are instrument-specific, while various calibration architectures cater to instrument stability and operational requirements, the fundamental techniques remain consistent. Similarly, DL models are tailored to specific instruments, but the model-building techniques can be applied to different instruments. In addition, we show over vicarious spatial sources our DL calibration provides reasonable calibrated antenna temperature values in comparison to SMAP values. This model has the potential to provide more accurate antenna temperature values in case if prelaunch data are used together with post-launch data for the calibration. Future studies of DL-based calibration can be trained and tested over SMAP's CAL/VAL sites if a sensor providing antenna temperature information is available [51], [52]. The computational time of a DL-based

calibrator can hold significant importance in the context of real-time processing. Depending on the specific scan duration during descending and ascending orbits for radiometers, additional optimization efforts and the potential implementation of specialized DL chips may become necessary.

## VI. SUMMARY AND CONCLUSION

This study showcases the capability of calibrating radiometers using DL technique, leveraging reduced reference information and 2-D antenna counts divided into time and frequency subbands. This study established five unique training scenarios containing the features from antenna observation power, reference and ND power and physical temperature, radiometer elements losses, and temperature. We have demonstrated that a radiometer can be calibrated with less or no information from the reference unit. The low RMSE and high R<sup>2</sup> value show that this study's robust DL-calibrator can contribute to more antenna observation within a footprint which might help to reduce radiometric uncertainty and solve spatial variability. Among the training scenario, cases 1 and 4 provides the best performance because of the availability of some reference and ND power information. SMAP level 1A and level 1B products are used in this study to understand the effectiveness of this DL-based model with different spatial and temporal distributions. SMAP's antenna temperature is considered ground truth for this study and helped in updating the parameters during the training phase. To understand model does not overfit, this study employs three different CV techniques—train-test split, K-fold, and time-based, incorporating samples from both land and landwater mix. Among them, samples comprising land-water mix help with the dynamic range and provide better performance. Analysis has shown that a DL-based calibrator could be an attractive consideration to calibrate radiometers for future Earth observation and weather satellites.

# REFERENCES

- N. Grody, "Remote sensing of atmospheric water content from satellites using microwave radiometry," *IEEE Trans. Antennas Propag.*, vol. 24, no. 2, pp. 155–162, Mar. 1976.
- [2] D. M. Le Vine, A. J. Griffis, C. T. Swift, and T. J. Jackson, "ESTAR: A synthetic aperture microwave radiometer for remote sensing applications," *Proc. IEEE Proc. IRE*, vol. 82, no. 12, pp. 1787–1801, Dec. 1994.
- [3] C. S. Ruf, C. T. Swift, A. B. Tanner, and D. M. Le Vine, "Interferometric synthetic aperture microwave radiometry for the remote sensing of the earth," *IEEE Trans. Geosci. Remote Sens.*, vol. 26, no. 5, pp. 597–611, Sep. 1988.
- [4] D. L. Vine and N. Skou, "Microwave radiometer systems: Design and analysis," Artech, 2006.
- [5] X. Xiong and W. Barnes, "An overview of MODIS radiometric calibration and characterization," Adv. Atmospheric Sci., vol. 23, pp. 69–79, 2006.
- [6] C. S. Ruf, "Characterization and correction of a drift in calibration of the TOPEX microwave radiometer," *IEEE Trans. Geosci. Remote Sens.*, vol. 40, no. 2, pp. 509–511, Feb. 2002.
- [7] F. T. Ulaby, R. K. Moore, and A. K. Fung, "Microwave remote sensing: Active and passive. volume 1 - microwave remote sensing fundamentals and radiometry," 1981.
- [8] C. S. Ruf, "Detection of calibration drifts in spaceborne microwave radiometers using a vicarious cold reference," *IEEE Trans. Geosci. Remote Sens.*, vol. 38, no. 1, pp. 44–52, Jan. 2000.
- [9] J. R. Piepmeier, L. Hong, and F. A. Pellerano, "Aquarius L-band microwave radiometer: 3 years of radiometric performance and systematic effects," *IEEE J. Sel. Topics Appl. Earth Observ. Remote Sens.*, vol. 8, no. 12, pp. 5416–5423, Dec. 2015.

- [10] J. Font et al., "SMOS: The challenging sea surface salinity measurement from space," *Proc. IEEE*, vol. 98, no. 5, pp. 649–665, May 2010.
- [11] L. L. Fu and B. J. Haines, "The challenges in long-term altimetry calibration for addressing the problem of global sea level change," Adv. Space Res., vol. 51, no. 8, pp. 1284–1300, 2013.
- [12] M. Ogut, X. Bosch-Lluis, and S. C. Reising, "Deep learning calibration of the high-frequency airborne microwave and millimeter-wave radiometer (HAMMR) instrument," *IEEE Trans. Geosci. Remote Sens.*, vol. 58, no. 5, pp. 3391–3399, May 2020.
- [13] M. Ogut, X. Bosch Lluis, and S. C. Reising, "A deep learning approach for microwave and millimeter-wave radiometer calibration," *IEEE Trans. Geosci. Remote Sens.*, vol. 57, no. 8, pp. 5344–5355, Aug. 2019.
- [14] M. Andrews et al., "The ultra-wideband software defined microwave radiometer (UWBRAD) for ice sheet subsurface temperature sensing: Calibration and campaign results," in *Proc. IEEE Int. Geosci. Remote Sens. Symp.*, 2017, pp. 237–240.
- [15] D. Entekhabi et al., "SMAP handbook-soil moisture active passive: Mapping soil moisture and freeze/thaw from space," JPL Pub., Pasadena, CA, USA, 2014.
- [16] J. R. Piepmeier, E. J. Kim, P. Mohammed, J. Peng, and C. Ruf, 2017, "SMAP L1A radiometer time-ordered parsed telemetry, version 2," Nat. Snow Ice Data Center, Boulder, CO, USA, doi: 10.5067/JGV8EY3FGAH1.
- [17] J. R. Piepmeier et al., 2020, "SMAP L1B radiometer half-orbit timeordered brightness temperatures, version 5," Nat. Snow Ice Data Center, Boulder, CO, USA, doi: 10.5067/ZHHBN1KQLI20.
- [18] "SMAP L1A Radiometer Time-ordered parsed telemetry, version 2 National Snow and Ice Data Center." Accessed: Jun. 5, 2023. [Online]. Available: https://nsidc.org/data/SPL1AP/versions/2
- [19] "SMAP L1B Radiometer half-orbit time-ordered brightness temperatures, version 5 | National Snow and Ice Data Center." Accessed: Jun. 5, 2023. [Online]. Available: https://nsidc.org/data/SPL1BTB/versions/5
- [20] D. Entekhabi et al., "The soil moisture active passive (SMAP) mission," Proc. IEEE Proc. IRE, vol. 98, no. 5, pp. 704–716, May 2010.
- [21] J. R. Piepmeier et al., "SMAP L-band microwave radiometer: Instrument design and first year on orbit," *IEEE Trans. Geosci. Remote Sens.*, vol. 55, no. 4, pp. 1954–1966, Apr. 2017.
- [22] J. Peng et al., "Soil moisture active/passive (SMAP) L-band microwave radiometer post-launch calibration upgrade," *IEEE J. Sel. Top*ics Appl. Earth Observ. Remote Sens., vol. 12, no. 6, pp. 1647–1657, Jun. 2019.
- [23] S. K. Chan et al., "Development and assessment of the SMAP enhanced passive soil moisture product," *Remote Sens. Environ.*, vol. 204, pp. 931–941, 2018.
- [24] J. Piepmeier, P. Mohammed, G. De, A. E. Kim, J. Peng, and C. Ruf, "Soil moisture active passive (SMAP) algorithm theoretical basis document (ATBD) SMAP calibrated, time-ordered brightness temperatures L1B TB data product," Jet Propulsion Lab., California Inst. Technol., Pasadena, CA, USA, 2014.
- [25] G. Macelloni et al., "CryoRad: A low-frequency wideband radiometer mission for the study of the cryosphere," in *Proc. IEEE Int. Geosci. Remote Sens. Symp.*, 2018, pp. 1998–2000.
- [26] J. T. Johnson et al., "The ultra-wideband software-defined radiometer (UWBRAD) for ice sheet internal temperature sensing: Results from recent observations," in *Proc. IEEE Int. Geosci. Remote Sens. Symp.*, 2016, pp. 7085–7087.
- [27] J. R. Piepmeier et al., "Radio-frequency interference mitigation for the soil moisture active passive microwave radiometer," *IEEE Trans. Geosci. Remote Sens.*, vol. 52, pp. 761–775, Jan. 2014.
- [28] A. M. Alam, M. Kurum, and A. C. Gurbuz, "High-resolution radio frequency interference detection in microwave radiometry using deep learning," in *Proc. IEEE Int. Geosci. Remote Sens. Symp.*, 2023, pp. 6779–6782.
- [29] P. N. Mohammed and J. R. Piepmeier, "Microwave radiometer RFI detection using deep learning," *IEEE J. Sel. Topics Appl. Earth Observ. Remote Sens.*, vol. 14, pp. 6398–6405, 2021.
- [30] A. M. Alam, A. C. Gurbuz, and M. Kurum, "SMAP radiometer RFI prediction with deep learning using antenna counts," in *Proc. IEEE Int. Geosci. Remote Sens. Symp.*, 2022, pp. 8016–8019.
- [31] W. Al-Qwider, A. M. Alam, M. Mehedi Farhad, M. Kurum, A. C. Gurbuz, and V. Marojevic, "Software radio testbed for 5G and L-band radiometer coexistence research," in *Proc. IEEE Int. Geosci. Remote Sens. Symp.*, 2023, pp. 596–599.
- [32] Z. Li, F. Liu, W. Yang, S. Peng, and J. Zhou, "A survey of convolutional neural networks: Analysis, applications, and prospects," *IEEE Trans. Neural Netw. Learn. Syst.*, vol. 33, no. 12, pp. 6999–7019, Dec. 2022.
- [33] J. Gu et al., "Recent advances in convolutional neural networks," Pattern Recognit., vol. 77, pp. 354–377, 2018.

- [34] S. Albawi, T. A. Mohammed, and S. Al-Zawi, "Understanding of a convolutional neural network," in *Proc. Int. Conf. Eng. Technol.*, 2017, pp. 1–6.
- [35] H. Perez and J. H. Tah, "Improving the accuracy of convolutional neural networks by identifying and removing outlier images in datasets using t-SNE," *Mathematics*, vol. 8, no. 5, 2020, Art. no. 662.
- [36] A. A. Soofi and A. Awan, "Classification techniques in machine learning: Applications and issues," J. Basic Appl. Sci, vol. 13, pp. 459–465, 2017.
- [37] L. Weng et al., "Towards fast computation of certified robustness for ReLU networks," in *Proc. Int. Conf. Mach. Learn.*, 2018, pp. 5276–5285.
- [38] S. Santurkar, D. Tsipras, A. Ilyas, and A. Madry, "How does batch normalization help optimization?," in *Proc. Adv. Neural Inf. Process. Syst.*, 2018, vol. 31, pp. 2488–2498.
- [39] Z. Zhang, "Improved adam optimizer for deep neural networks," in Proc. IEEE/ACM 26th Int. Symp. Qual. Service, 2018, pp. 1–2.
- [40] A. Senior, G. Heigold, M. A. Ranzato, and K. Yang, "An empirical study of learning rates in deep neural networks for speech recognition," in *Proc. IEEE Int. Conf. Acoust., Speech Signal Process.*, 2013, pp. 6724–6728, doi: 10.1109/ICASSP.2013.6638963.
- [41] Y. Yao, L. Rosasco, and A. Caponnetto, "On early stopping in gradient descent learning," *Constructive Approximation*, vol. 26, no. 2, pp. 289–315, 2007.
- [42] S. Yan et al., "An overview of overfitting and its solutions," J. Physics: Conf. Ser., vol. 1168, 2019, Art. no. 022022.
- [43] S. T. Brown and C. S. Ruf, "Determination of an amazon hot reference target for the on-orbit calibration of microwave radiometers," *J. Atmospheric Ocean. Technol.*, vol. 22, no. 9, pp. 1340–1352, 2005.
- [44] I. Pietroni, S. Argentini, and I. Petenko, "One year of surface-based temperature inversions at dome C., antarctica," Boundary-Layer Meteorology, vol. 150, pp. 131–151, 2014.
- [45] G. Macelloni, M. Brogioni, P. Pampaloni, A. Cagnati, and M. R. Drinkwater, "DOMEX 2004: An experimental campaign at dome-c antarctica for the calibration of spaceborne low-frequency microwave radiometers," *IEEE Trans. Geosci. remote Sens.*, vol. 44, no. 10, pp. 2642–2653, Oct. 2006.
- [46] N. Patel, L. Hong, W. Jones, and S. Vasudevan, "Evaluation of the Amazon rain forrest as a distributed target for satellite microwave radiometer calibration," in *Proc. IEEE Int. Symp. Geosci. Remote Sens.*, 2006, pp. 85–88.
- [47] A. Paszke et al., "PyTorch: An imperative style, high-performance deep learning library," in *Proc. Adv. Neural Inf. Process. Syst.*, 2019, vol. 32, pp. 8024–8035.
- [48] F. Pedregosa et al., "Scikit-learn: Machine learning in python," J. Mach. Learn. Res., vol. 12, pp. 2825–2830, 2011.
- [49] M. M. Farhad, S. Biswas, A. M. Alam, A. C. Gurbuz, and M. Kurum, "SDR based agile radiometer with onboard RFI processing on a small UAS," in *Proc. IEEE Int. Geosci. Remote Sens. Symp.*, 2023, pp. 4368–4371.
- [50] A. M. Alam, M. Kurum, and A. C. Gurbuz, "Radio frequency interference detection for SMAP radiometer using convolutional neural networks," *IEEE J. Sel. Topics Appl. Earth Observ. Remote Sens.*, vol. 15, pp. 10099–10112, Nov. 2022, doi: 10.1109/JSTARS.2022.3223198.
- [51] A. Colliander et al., "Validation of SMAP surface soil moisture products with core validation sites," *Remote Sens. Environ.*, vol. 191, pp. 215–231, 2017.
- [52] S. K. Chan et al., "Assessment of the SMAP passive soil moisture product," *IEEE Trans. Geosci. Remote Sens.*, vol. 54, no. 8, pp. 4994–5007, Aug. 2016.



Ahmed Manavi Alam (Graduate Student Member, IEEE) received the B.S. degree in electrical and electronic engineering from the Bangladesh University of Engineering and Technology, Dhaka, Bangladesh, in 2019. He is currently working toward the Ph.D. degree in electrical and computer engineering with the Mississippi State University, Starkville, MS, USA.

He is currently working as a Research Assistant with the Information Processing and Sensing Laboratory. He was a machine learning intern at High Performance Computing Collaboratory. His research

interests include algorithm development of deep learning-based inverse problems and machine learning for remote sensing and physics aware deep learning. Prof. Alam is a Student Member of IEEE Geoscience and Remote Sensing Society. He was a finalist at the IGARSS 2022 Student Paper competition.



Mehmet Kurum (Senior Member, IEEE) received the B.S. degree in electrical and electronics engineering from Bogazici University, Istanbul, Türkiye, in 2003, and the M.S. and Ph.D. degrees in electrical engineering from George Washington University, Washington, DC, USA, in 2005 and 2009, respectively.

He held Postdoctoral and Research Associate positions with the Hydrological Sciences Laboratory, NASA Goddard Space Flight Center, Greenbelt, MD, USA. From 2016 to 2022, he was an Assistant Professor at Mississippi State University, Starkville, MS,

USA (MSU), and subsequently, he held the position of Associate Professor and the Paul B. Jacob Endowed Chair until 2023. Currently, he is an Associate Professor in Electrical and Computer Engineering with the University of Georgia, Athens, GA, USA, while also serving as an Adjunct Professor, MSU. His research focuses on recycling the radio spectrum to address the challenges of decreasing radio spectrum space for science while exploring entirely new microwave regions for land remote sensing.

Dr. Kurum is a Senior Member of IEEE Geoscience and Remote Sensing Society (GRSS) and a Member of U.S. National Committee for the International Union of Radio Science. Since 2021 he has been the Associate Editors for IEEE TRANSACTIONS ON GEOSCIENCE AND REMOTE SENSING and IEEE JOURNAL OF SELECTED TOPICS IN APPLIED EARTH OBSERVATIONS AND REMOTE SENSING. He was a recipient of the Leopold B. Felsen Award for excellence in electromagnetic in 2013 and the International Union of Radio Science (URSI) Young Scientist Award in 2014, and NSF CAREER award in 2022. He served as an Early Career Representative for the International URSI Commission F (Wave Propagation and Remote Sensing) from 2014–2021.



Mehmet Ogut (Member, IEEE) received the B.S. degree in electrical and electronics engineering from Bogazici University, Istanbul, Türkiye, in 2011, M.S degree in electrical engineering from the George Washington University, Washington, DC, USA, in 2013, and the Ph.D. degree in electrical engineering from Colorado State University (CSU), Fort Collins, CO, USA, in 2018.

He is currently working with NASA/Caltech Jet Propulsion Laboratory (JPL) in Pasadena, California, USA, as a Technologist in Microwave Instrument

Science Group. He is the CO-I and JPL lead of Ultra-Wideband Photonic Spectrometer for Planetary Boundary Layer Sensing funded under NASA Earth Science Technology Office (ESTO) Advanced Component Technology (ACT-20), the CO-I of Smart Ice Cloud Sensing (SMICES) high frequency radiometer (250-670 GHz), sounder (380 GHz) and radar (240 GHz) awarded under NASA ESTO IIP-19, the CO-I of Compact Fire Infrared Radiance Spectral Tracker (c-FIRST) funded by NASA ESTO IIP-21, the CO-I of the Ultra-Wide RF ACT-22 project. His research interests include design, testing, calibration, and analysis of microwave and millimeter-wave radar/radiometer instruments, developing innovative concepts in radiometry, artificial intelligence and photonic applications in remote sensing.

Dr. Ogut is the recipient of the 2023 best paper award from IEEE Transactions on Terahertz Science and Technology. He is a Member of Eta Kappa Nu, IEEE GRSS, and MTTS societies.



Ali C. Gurbuz (Senior Member, IEEE) received the B.S. degree in electrical engineering from Bilkent University, Ankara, Turkey, in 2003, and the M.S. and Ph.D. degrees in electrical and computer engineering from the Georgia Institute of Technology, Atlanta, GA, USA, in 2005 and 2008, respectively.

From 2003 to 2009, he researched compressive sensing-based computational imaging problems at Georgia Tech. He held faculty positions at TOBB University, Ankara, Türkiye, and University of Alabama, Tuscaloosa, AL, USA, between 2009 and 2017 where

he pursued an active research program on the development of sparse signal representations, compressive sensing theory and applications, radar and sensor array signal processing, and machine learning. Currently, he is an Assistant Professor with the Department of Electrical and Computer Engineering, Mississippi State University, Starkville, MS, USA, where he is co-Director of Information Processing and Sensing (IMPRESS) Laboratory.

Dr. Gurbuz was the recipient of The Best Paper Award for Signal Processing Journal in 2013 and the Turkish Academy of Sciences Best Young Scholar Award in Electrical Engineering in 2014, NSF CAREER award in 2021. He was an Associate Editor for several journals, such as Digital Signal Processing, EURASIP Journal on Advances in Signal Processing and Physical Communications.